ELSEVIER

#### Contents lists available at ScienceDirect

## Acta Materialia

journal homepage: www.elsevier.com/locate/actamat



## Laser Powder Bed Fusion of Defect-Free NiTi Shape Memory Alloy Parts with Superior Tensile Superelasticity



L. Xue<sup>a</sup>, K.C. Atli<sup>a</sup>, C. Zhang<sup>b</sup>, N. Hite<sup>a</sup>, A. Srivastava<sup>a</sup>, A.C. Leff<sup>c,d</sup>, A.A. Wilson<sup>c</sup>, D.J. Sharar<sup>c</sup>, A. Elwany<sup>b</sup>, R. Arroyave<sup>a</sup>, I. Karaman<sup>a,\*</sup>

- <sup>a</sup> Department of Materials Science and Engineering, Texas A&M University, College Station, Texas,77843
- b Wm Michael Barnes '64 Department of Industrial and Systems Engineering, Texas A&M University, College Station, TX, 77843
- <sup>c</sup> U.S. Army Research Laboratory, Adelphi, MD, 20783
- <sup>d</sup> General Technical Services, LLC, Wall, NJ, 07727, United States

#### ARTICLE INFO

#### Article history: Received 19 August 2021 Revised 11 February 2022 Accepted 21 February 2022 Available online 22 February 2022

Keywords: Additive manufacturing Laser powder bed fusion Shape memory alloys Process optimization Superelasticity

#### ABSTRACT

Laser powder bed fusion is a promising additive manufacturing technique for the fabrication of NiTi shape memory alloy parts with complex geometries that are otherwise difficult to fabricate through traditional processing methods. The technique is particularly attractive for the biomedical applications of NiTi shape memory alloys, such as stents, implants, and dental and surgical devices, where primarily the superelastic effect is exploited. However, few additively manufactured NiTi parts have been reported to exhibit superelasticity under tension in the as-printed condition, without a post-fabrication heat treatment, due to either persistent porosity formation or brittleness from oxidation during printing, or both. In this study, NiTi parts were fabricated using laser powder bed fusion and consistently exhibited room temperature tensile superelasticity up to 6% in the as-printed condition, almost twice the maximum reported value in the literature. This was achieved by eliminating porosity and cracks through the use of optimized processing parameters, carefully tailoring the evaporation of Ni from a Ni-rich NiTi powder feedstock, and controlling the printing chamber oxygen content. Crystallographic texture analysis demonstrated that the as-printed NiTi parts had a strong preferential texture for superelasticity, a factor that needs to be carefully considered when complex shaped parts are to be subjected to combined loadings. Transmission electron microscopy investigations revealed the presence of nano-sized oxide particles and Ni-rich precipitates in the as-printed parts, which play a role in the improved superelasticity by suppressing inelastic accommodation mechanisms for martensitic transformation.

© 2022 Acta Materialia Inc. Published by Elsevier Ltd. All rights reserved.

## 1. Introduction

Superelasticity (SE) and shape memory effect (SME) in Shape Memory Alloys (SMAs) originate from reversible martensitic phase transformations. Control of these transformations has enabled a number of important technologies, such as active biomedical devices, compact actuators, adaptive couplings and seismic damping functional/structural elements. For most of these applications, NiTi is the material of choice, as it is the most widely researched and commercially available SMA, in addition to its superior shape memory properties, biocompatibility and corrosion resistance. Unfortunately, NiTi is exceedingly challenging to machine and manufacture into parts of arbitrary geometry due to its high toughness and strain hardening [1–3]. Specialized machining techniques, such

E-mail address: ikaraman@tamu.edu (I. Karaman).

as cryogenic machining and electrical discharge machining (EDM), provide alternative fabrication methods, however they are costly and offer limited geometric complexity in the parts that they produce

Powder-bed fusion (PBF) [4–11] and directed energy deposition (DED) [12–18] additive manufacturing (AM) techniques have been extensively studied as routes toward the fabrication of nearnet-shape NiTi SMA parts, bypassing costly machining steps. PBF AM techniques such as laser-PBF (L-PBF) or electron beam melting (EBM) usually feature small beam size, require powders with finer size distribution, and rely on thinner powder bed layers, resulting in better surface finish and geometric accuracy. DED, on the other hand, offers a greater degree of design freedom, including changing the input powder composition during printing and can be used to repair or add additional material to existing components. In biomedical applications, control of surface finish is necessary in order to limit, for example, the release of (toxic) Ni [19] and substantial attention has thus been given to L-PBF of NiTi.

<sup>\*</sup> Corresponding author.

NiTi parts fabricated using AM have been reported to exhibit up to 10% compressive [11] and up to 8% tensile recoverable strain through SME [20], comparable to NiTi parts fabricated via conventional ingot metallurgy techniques. However, the starting powder for these parts is usually a relatively low Ni-rich NiTi powder (i.e. Ni < 50.5 at. %) and the printed parts typically have transformation temperatures above room temperature and do not display SE. Compared to SME, achieving SE in AM NiTi is exceedingly challenging. Firstly, to accomplish SE in AM NiTi, the printed parts should have an austenite finish (A<sub>f</sub>) temperature lower than the operating temperature--in biomedical applications this corresponds to body temperature. Beyond 50 at.% Ni, the transformation temperature(s) in binary NiTi SMAs decrease and to lower them to the required operating temperature in biomedical applications it is necessary to use a high Ni-rich NiTi powder feedstock (i.e. Ni > 50.7 at. %). Local temperatures during AM of NiTi can easily result in significant preferential evaporation since Ni has a vapor pressure about three orders of magnitude higher than that of Ti at relevant temperatures. This can alter the chemical makeup of the deposited material and significantly affecting its transformation temperatures [4,7,9,20-27]. Therefore, processing parameters must be carefully selected to achieve the final desired Ni content, and thus, the transformation temperatures of the printed NiTi parts. Secondly, even if the processing conditions can be controlled to ensure target transformation temperatures in the as-printed part, desired SE behavior may not be achieved. This occurs when the strength of the matrix is not high enough, as the critical stress inducing the martensitic transformation also leads to dislocation plasticity in the parent phase during loading. Thirdly, the epitaxial growth between successive layers, the presence of porosity (due to poorly controlled manufacturing conditions) and/or non-metallic inclusions (due to poor control of the atmosphere in the build chamber) and the generation of residual stresses may lead to embrittlement of the part, as it fails before exhibiting SE effect. To date, a few studies have reported SE behaviour in AM NiTi samples under both compressive and tensile loading [4,12,28-37]. However, the maximum tensile recoverable strain in as-fabricated condition was at most only 3%, accompanied by a relatively large residual strain of about 1% [32], partly due to the abovementioned issues. We note that characterization of the tensile properties of AM NiTi is crucial since as-printed parts are more prone to fracture from defects (e.g., porosity and micro cracks) in tension as compared to that under

During L-PBF, excessive energy input can trap the vaporized constituent elements within the melt pool causing spherical pores, while insufficient energy input may lead to unmelted powder between the melt pools or weak bonding (microcracks) between layers. Although a porous structure [5,19,29] may be preferred for biomedical implants for the low stiffness, pores may lead to early failure through crack initiation and propagation, bringing serious consequences especially in applications requiring multiple loading or actuation cycles. Due to the characteristic high cooling rates associated with the L-PBF processes and resulting steep temperature gradients in the printed parts, residual stresses may also result in unpredictable mechanical behaviour or cause macroscopic defects such as warping and delamination. Recent studies have suggested the use of strip scanning patterns with shorter scanning length (also known as vector length) to induce smaller thermal gradients [38]. Parts printed with such scanning patterns were reported to exhibit tensile ductility levels as high as 16% [38]. The highest tensile ductility reported so far for AM NiTi is about 20% which was achieved by utilizing a similar scanning pattern together with 25 ppm oxygen level in the build chamber [20], which is much lower than the 500 ppm suggested by ASTM F2063-05 [39].

Control of the microstructure in AM NiTi is of paramount importance in order to improve the thermomechanical properties to

a level close to those of NiTi fabricated by conventional ingot metallurgy. Texture has been known to greatly affect functional properties in single and polycrystalline NiTi [40–42], and studies have revealed the evolution of specific textures in the direction of highest thermal gradient during the intrinsic epitaxial solidification in AM processes [6,31,43]. Utilizing a smaller hatch spacing between laser tracks during printing has also been reported to result in a stronger texture and grain refinement [31].

In wrought Ni-rich NiTi, solution heat treatment to reach a matrix without secondary phases followed by aging heat treatment at 300 to 550°C [44] is commonly used to modify the size and distribution of Ni-rich precipitates, strengthen the matrix against defect generation mechanisms and achieve SE. Although the effects of aging on functional properties have been widely studied in NiTi fabricated using conventional ingot metallurgy [45-49], choosing the appropriate heat treatment parameters for AM NiTi is a challenging task, since the Ni content of the as-fabricated parts will usually be different than the starting powder and may vary depending on the selection of the process parameters. Post printing heat treatments have been successfully used for AM NiTi parts to grow Ni-rich precipitates [12] and improve SE [7,50] of Ni-rich NiTi. However, regardless of the quality of the protective atmosphere, formation of oxides such as TiO<sub>2</sub> or Ti<sub>4</sub>Ni<sub>2</sub>O<sub>x</sub> is a persistent problem during heat treatments at relatively high temperatures (e.g. solution heat treatment) that may impair shape memory behaviour and durability. Hence, achieving good and stable SE in as-printed parts, without any post printing heat treatments is a technological challenge that must be overcome for practical use of AM NiTi parts.

There are multiple factors that need to be considered during L-PBF of NiTi in order to fabricate defect-free and fully dense parts, such as starting powder composition and quality, the choice of scanning strategy, and selection of processing parameters. Extensive research has been devoted to the optimal selection of processing parameters in different platforms, however it is known that one set of parameters optimized for one AM platform may not always produce the same results in another AM platform due to hardware differences. Therefore, there is a need for rapid AM process parameter optimization methods to select the best process parameters for each AM platform. To address this issue, we have recently reported a robust process optimization framework [51] in order to rapidly select the optimum process parameters to fabricate near fully dense AM parts. This framework utilizes a simple analytical model, i.e. the Eagar-Tsai (E-T) model [51,52] to predict melt pool dimensions during the L-PBF process as a function of material properties and processing parameters, paired with single laser track experiments to identify the window of feasible process parameters for different alloys including NiTi. This framework saves considerable effort in parameter optimization as compared to performing experiments spanning the full parameter space for a given powder type.

In a recent study by the authors [37], defect free NiTi parts could be printed starting with lower Ni content NiTi powders and using a process optimization framework to construct an optimum printability / processing map. The resulting samples exhibited superior ductility and SME. However, the parts had poor SE due to the lack of coherent Ni-rich precipitates that act as strengthening agents against defect generation mechanisms. In addition, the crystallographic texture was not characterized. The present study demonstrates the highest tensile SE achieved to date in L-PBF of a high Ni-rich NiTi, owing to the selection of optimal process parameters using the same process optimization framework for eliminating defects, controlling crystallographic texture, and forming Ni-rich nanoprecipitates. Lowering the oxygen level in the printing chamber was also found to yield superior tensile ductility and SE, while an increase in the volumetric energy density was revealed to mitigate macroscopic defects such as cracks, warping and delam-

ination. Extensive microstructural characterization including electron backscatter diffraction (EBSD) and transmission electron microscopy (TEM) analysis was conducted to reveal the underlying mechanisms of the superior SE and the effects of chamber oxygen content. Also reported in this study are thermal conductivity values of parts printed with different processing parameters and printing chamber oxygen content, which is extremely scarce for AM NiTi in literature and holds great importance for actuation and thermal management applications such as elastocaloric cooling.

#### 2. Experimental and Computational Methods

#### 2.1. Powder characterization

A NiTi shape memory alloy (SMA) ingot with a nominal composition of Ni<sub>51.2</sub>Ti<sub>48.8</sub> (at. %) was acquired from Fort Wayne Metals and then gas-atomized by Nanoval GmbH & Co. KG. Solution heat treatment of powder samples was performed at 950°C for 24 h in quartz tubes with protective argon atmosphere followed by quenching and breaking the tubes in water at room temperature. A TA instruments Q2000 differential scanning calorimeter (DSC) was used to measure the transformation temperatures of the asreceived and solutionized powders. Two thermal cycles were run between -150°C and 150°C at a heating/cooling rate of 10°C/min. Transformation temperatures were determined from the second cycle results using the tangent line interception method following ASTM F2004-17 [53]. A FEI Quanta 600 FE scanning electron microscope (SEM) operated at 20 kV was used to investigate the morphology and size distribution of the powder particles.

#### 2.2. Generation of the printability map and additive manufacturing

A 3D Systems ProX DMP 200 L-PBF system with a fibre laser of 1070 nm wavelength and beam diameter of 80  $\mu$ m was used to fabricate the NiTi parts. Equiatomic NiTi (i.e. Ni<sub>50</sub>Ti<sub>50</sub> (at. %)) plates were used as substrates for the prints and were sandblasted with 50  $\mu$ m aluminum oxide prior to printing in order to achieve better powder spreading and coverage of the substrate. Layer thickness (t) was set to 32  $\mu$ m during printing of single tracks, cubes, and rectangular prisms to have at least 80% of the powder within the layer based on the particle size distribution (PSD) information.

The Eagar-Tsai (E-T) analytical model was utilized to predict melt pool dimensions during L-PBF as a function of material properties and processing parameters. The initial predictions of the E-T model were made based on nominal processing parameters P (laser power), v (scan speed) and the size of the laser beam, and the material properties of NiTi collected from literature. The reader is referred to [37] for details on the selection of different material properties used in the E-T model. With the measured melt pool dimensions from the single-track experiments, the model was calibrated in order to more precisely predict the melt pool dimensions corresponding to different P and v values. The printability map could then be constructed taking into consideration the different regions (e.g. keyhole region, printable region, lack of fusion and balling regions) bounded by specific ratios of d, w and t, where d is the melt pool depth, w is the melt pool width, and t is the layer thickness (set to  $d_{80}$  of the powder) (Fig. 1). For instance, to define the "good" printable region on the printability map, d was selected larger than the powder thickness, t, (Fig. 1a) ensuring enough remelting of previously printed layer to avoid lack of fusion (Fig. 1d), but not exceeding w/1.5 to cause potential keyholing porosity (Fig. 1b). As shown in Fig. 1a, the single track classified as "good" shows continuity along the length and enough penetration into the substrate, which indicates potentially good remelting of the previously sintered layer. An l/w ratio, where l is the length of the melt pool, greater than 2.3 was chosen as the initial estimate for the balling defect criterion (Fig. 1c) to generate the initial printability map. The balling region was determined by the support vector machines (SVM) classifier with the cubic polynomial kernel constructed according to the single track experimental results, following the method introduced in [51], from which the balling and continuous tracks were distinctly identified.

10 mm long single tracks with 1 mm intervals were printed on an equiatomic NiTi substrate using 66 different P and v combinations, with a range of (P,v) = (40-240 W: 0.08-2.33 m/s). Top-view SEM images were taken from the middle of each single track and six width measurements were conducted to assess the continuity of the tracks. Cross-section samples of the single tracks were prepared using wire electrical discharge machining (wire-EDM) and then grinding with up to 1200 grit sandpaper followed by a final polishing with water based colloidal silica  $(0.25 \ \mu\text{m})$  suspension. The polished surfaces were then etched with an etchant of 1 part HF, 2 parts HNO $_3$  and 10 parts distilled water for 15 s to reveal the grains and the melt pool shapes. Optical microscopy images of the single track cross-sections were taken using a Keyence VH-X digital microscope and d was calculated as the average of three different cross-section measurements.

Following the printing of the single tracks, six cube samples with dimensions of  $10 \times 10 \times 10 \text{ mm}^3$  were printed using a range of process parameters selected from the "good" region on the printability map which also yielded high quality single tracks devoid of any keyholing or balling defects. After a visual inspection of the overall quality of the printed cubes, confirming that no significant porosity existed, and taking into account the transformation temperatures measured for each cube, the process parameter set that resulted in the best print quality and yielded a fully austenitic structure at room temperature was used to scale up and print  $30 \times 10 \times 10 \text{ mm}^3$  rectangular prisms to yield dog-bone tension specimens for mechanical and SE characterization. Finally, in order to assess the effect of build chamber oxygen content on the mechanical and SE properties, rectangular prisms were printed at a lower chamber O2 content of 100 ppm compared to the 500 ppm for all other prints. For both cubes and rectangular prisms, a bidirectional scan pattern with a 45° angle to the edge of the prints and a 90° hatch rotation between the layers was employed during printing.

#### 2.3. Density and porosity measurements

Density of the as-printed rectangular prisms was measured using Archimedes' method following ASTM B962-17 [54]. A quantitative density comparison of the as-printed parts was also conducted by the porosity analysis of SEM images, taken from the cross-sectional surfaces parallel to the build direction. These images were then processed using ImageJ software to calculate the porosity amount.

## 2.4. Thermal properties and thermomechanical characterization

3 mm diameter x 1 mm thick DSC samples were wire-EDM cut from the as-printed rectangular prisms. DSC samples were initially used to find the transformation temperatures of as-printed parts. 2 thermal cycles were run between -150°C and 150°C at a heating/cooling rate of 10°C/min. The samples were subsequently solutionized at 800°C for 1 h to dissolve any possible secondary phases and retested for 2 more thermal cycles in an effort to indirectly determine the matrix Ni content based on the martensite start (M<sub>s</sub>) temperatures as outlined in [55] due to the difficulties associated with detecting small changes in Ni content through conventional chemical analysis.

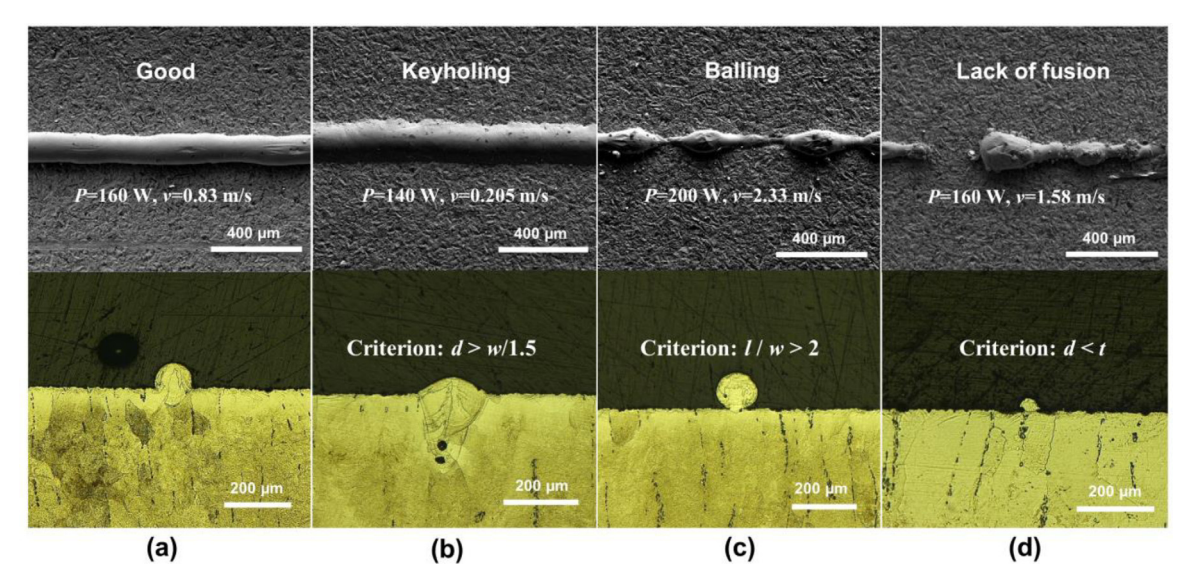


Fig. 1. Single track top-view SEM images and cross-sectional optical microscopy (OM) images displaying the examples of the single tracks with (a) good print quality, (b) keyholing defect, (c) balling defect and (d) lack of fusion defect.

Thermomechanical testing was performed using a servo hydraulic MTS test frame with heating and cooling capability. Dogbone tension specimens with gage dimensions of 8 mm  $\times$  3 mm × 1 mm were wire-EDM cut from the as-printed rectangular prisms, such that the loading axis was parallel to the long edge of the prisms, and the width direction is perpendicular to the build direction. Incremental loading-unloading tests were conducted on these dog-bone tension specimens at a nominal strain rate of 5  $\times$  10<sup>-4</sup> s<sup>-1</sup> and at different temperatures above the A<sub>f</sub> temperature for characterizing the SE of the as-printed parts. A spring-loaded MTS high-temperature extensometer was attached to the gage section of the samples to monitor the tensile strain during thermomechanical testing. Specimens were initially loaded to 0.5% strain, unloaded and the loading-unloading cycles continued with 1% increments until failure occurred. To characterize the transformation stress as a function of temperature, specimens were loaded at different temperatures to 1% strain, unloaded and heated up to 100°C for full recovery, a temperature well above the Af temperature.

## 2.5. Phase analysis and crystallographic texture study

Two cross-sectional samples (perpendicular to and along the build direction) wire-EDM cut from the rectangular prisms were mechanically ground and polished using the same procedure used to prepare optical microscopy samples. Polished samples were then heated to 100°C and cooled down to RT to recover any residual martensite before running the X-ray diffraction (XRD) and EBSD analyses. Phase analysis was conducted using a Bruker D8 Discover X-ray Diffractometer equipped with a Vantec 500 detector and Cu  $K_{\alpha}$  (0.15406 nm) X-ray source. The texture and microstructure of these surfaces were investigated utilizing a TESCAN FERA SEM with EBSD detector from Oxford Instruments. Large sample areas were analysed using step size of 1.3 µm whereas a detailed analysis of smaller areas was performed using a step size of 0.1 µm with a tilt angle of 70°. The EBSD raw data was processed using Aztec Crystal software to plot inverse pole figure maps, pole figures, and kernel average misorientation (KAM) maps. For the evaluation, misorientations greater than 15° were defined as high-angle grain boundaries whereas those greater than 2° but less than 15° were defined as low-angle grain boundaries. KAM was calculated using the 3rd

order neighbors (kernel size) and maximum misorientation angle of  $5^{\circ}$ .

#### 2.6. Transmission electron microscopy (TEM)

TEM experiments were performed on the cross-section surfaces (both perpendicular and parallel to the build direction) from rectangular prisms to investigate any possible oxide inclusions and precipitate formation that may affect the thermomechanical properties of the printed parts. TEM foils were prepared by initially mechanical grinding of slices wire EDM-cut from the rectangular prisms down to 50  $\mu m$ , followed by punching of foils with a diameter of 3 mm. Foils were finally ion milled using a Gatan PIPS II at -165 °C. A JEOL ARM200F scanning transmission electron microscope (STEM) was used at an accelerating voltage of 200 kV. STEM energy-dispersive X-ray spectroscopy (EDS) was also used to detect the chemical composition of the precipitates.

## 2.7. Thermal diffusivity measurements

Thermal diffusivity measurements were performed on 1 mm thick.  $10 \times 10$  mm square cross sections which were wire-EDM cut from the rectangular prisms. From each prism, seven samples were cut normal to the build direction from varying build heights with 0.33 mm between samples. Additionally, three samples with faces parallel to the build direction were cut from each prism. It should be noted that since thermal diffusivity is measured through the thickness of the specimen, when a surface normal to the build direction is characterized, the measured diffusivity is parallel to the build direction. All samples underwent thermal diffusivity measurement using a TA Instruments DXF 200 high-speed Xenon-pulse delivery source and solid-state PIN detector. Measurements were taken at approximately 50 °C temperature intervals as the samples were heated from -150 °C to 150 °C. The measurements were repeated during cooling from 150 °C to -150 °C. Specific heat capacity values were obtained from the respective DSC curves via the sapphire standard method. Thermal conductivity was then calculated according to the equation:  $k = \alpha \cdot \rho \cdot c_p$ , where k is thermal conductivity,  $\alpha$  is thermal diffusivity,  $\rho$  is density, and  $c_p$  is specific heat capacity.

Fig. 2 below shows a flowchart summarizing the experimental methods utilized in this study.

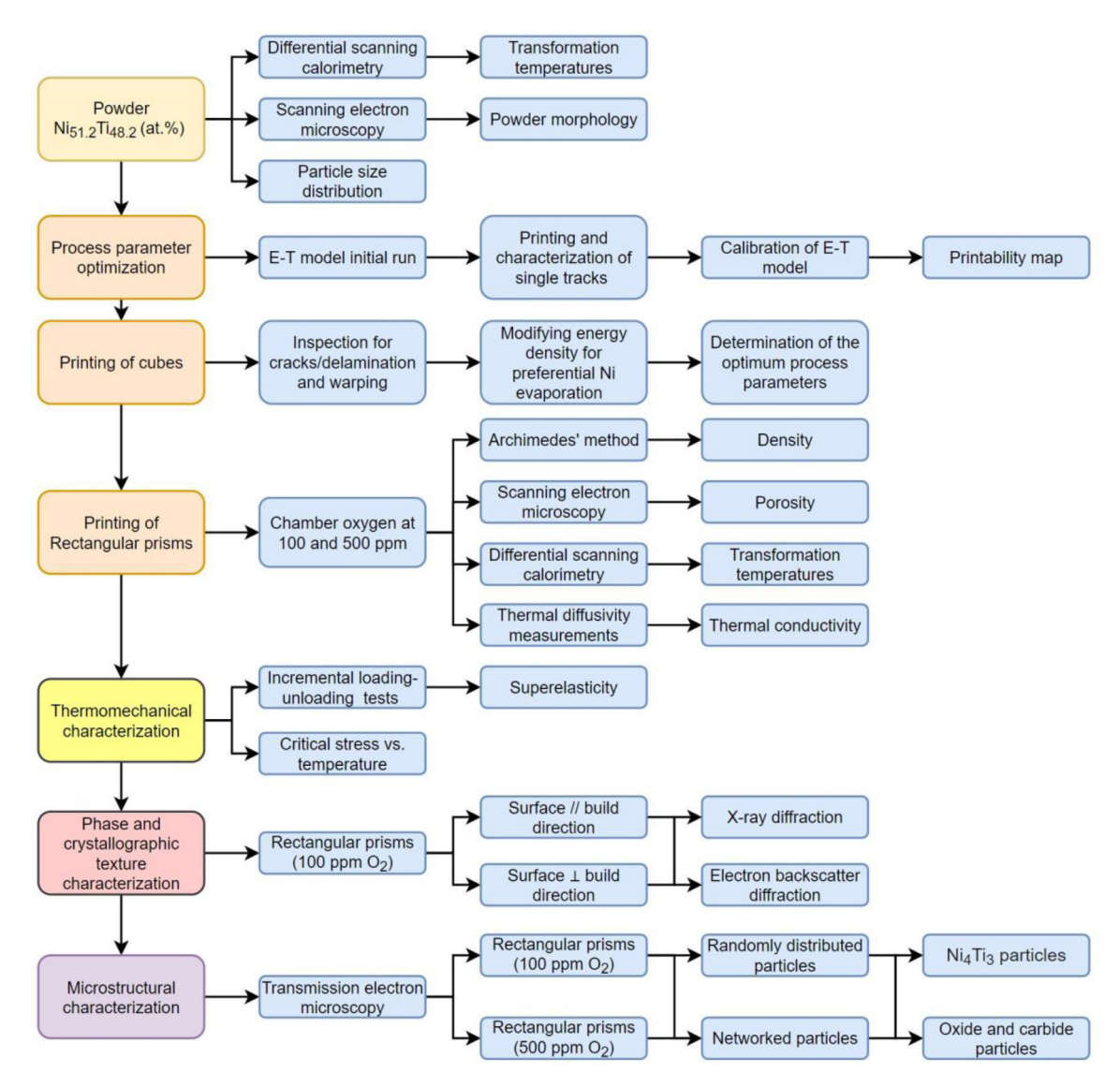


Fig. 2. Flowchart summarizing the experimental methods used and properties/features measured/detected in this study.

#### 3. Experimental Results

## 3.1. Powder characterization

Based on SEM observations, as-received NiTi powder has mostly spherical particles with sizes ranging from 5  $\mu$ m to 70  $\mu$ m (Fig. 3a and Fig. 3b).  $d_{50}$  and  $d_{80}$  values are 20  $\mu$ m and 32  $\mu$ m, respectively (Fig. 3c). DSC results indicate that the as-received powder exhibits a broad peak during reverse transformation around -10°C (Fig. 3d). After solutionizing at 900°C for 1h in a protective argon atmosphere, no transformation peaks were observed down to -150°C, indicating the Ni content in this powder would be at least 51 at. % based on the  $M_{\rm S}$  temperature prediction with respect to Ni content [56].

## 3.2. Single tracks and the printability map

Single tracks were printed to investigate the quality and the morphology of the melt pools resulting from different laser power (P) and scan speed (v) combinations as previously shown in Fig. 1. Melt pool depth (d) and width (w) values showed an increasing trend with increasing linear energy density (LED = P/v) (Fig. 4a

and Fig. 4b). In general, for the combinations resulting in relatively low levels of LED, the laser was not able to melt the entire powder layer and left no tracks on the substrate or resulted in tracks with non-uniform width and discontinuity, causing the lack of fusion phenomenon (Fig. 1d). On the other hand, when the LED was relatively high, vaporization of elemental constituents resulted in trapped gases within the melt pools, leading to the keyholing defect (Fig. 1d). It is also observed that the melt pool becomes unstable when P and v are both high, and the single tracks break into discontinuous droplets on the substrate, causing the balling phenomenon (Fig. 1c).

Once the calibrated printability map (Fig. 4c) was obtained based on the measured single tracks following the methodology summarized in [37, 51, 57], four P and v combinations (Table 1) were selected from the "Good" region (Fig. 4c) that yielded continuous tracks with reasonable penetration to the substrate (e.g. deeper than the layer thickness, t). The maximum value of the hatch spacing between adjacent laser tracks was calculated using the formula  $h_{max} = w \sqrt{1 - \frac{t}{(t+d)}}$  [51] to ensure sufficient overlap between adjacent tracks and provide integrity to the single layer.

At first inspection of Cubes #1 to #4 (Fig. 5), macroscopic defects such as delamination from the substrate, cracks and warping

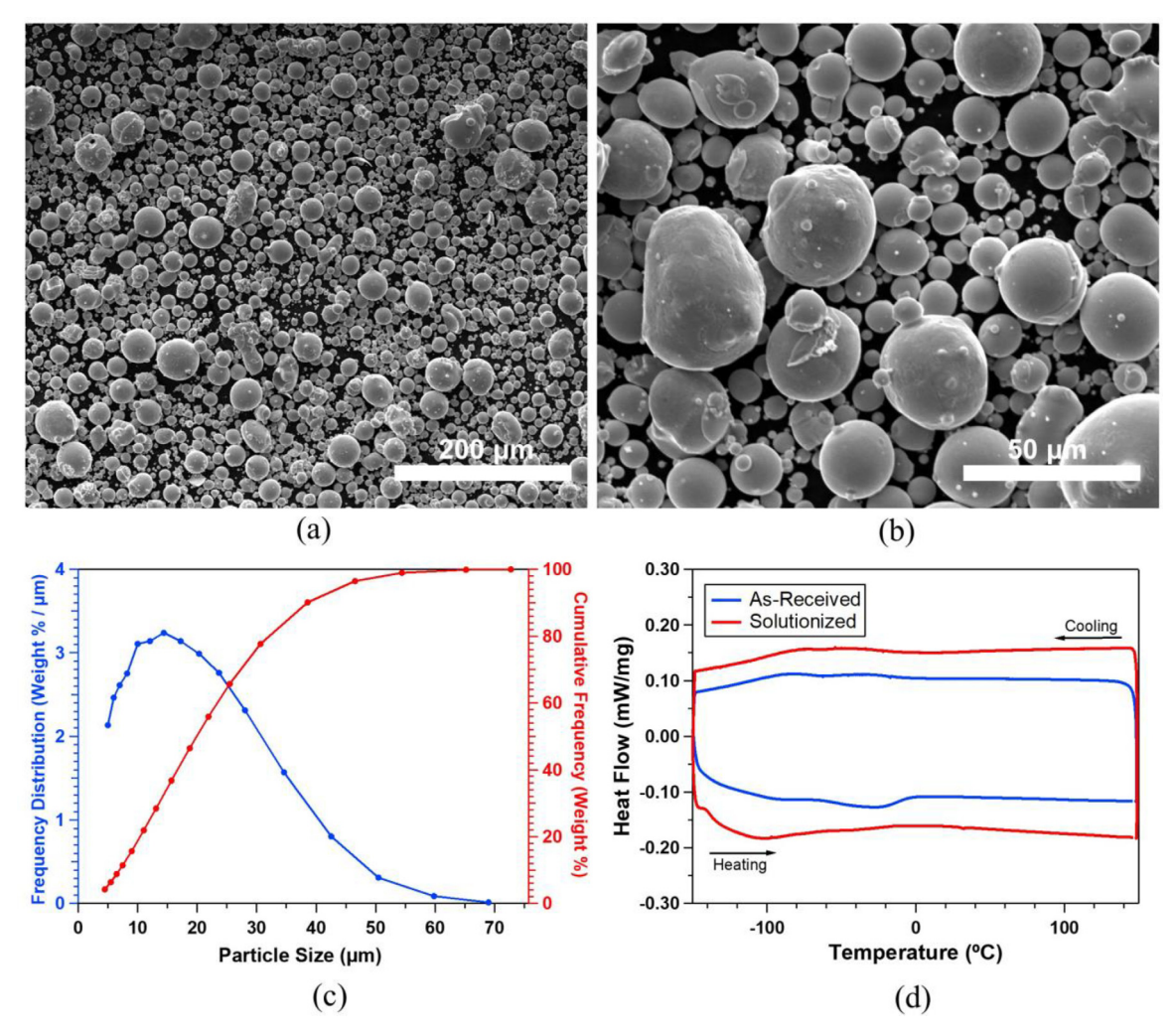


Fig. 3. (a) Low-magnification and (b) higher magnification SEM images of the as-received Ni<sub>51,2</sub>Ti<sub>48,8</sub> powder. (c) Particle size distribution (PSD) of the powder and (d) differential scanning calorimetry (DSC) results of both as-received powder and powder after a solution heat treatment at 950°C for 24h.

**Table 1** Processing parameters used for printing  $10 \times 10 \times 10 \text{ mm}^3$  cubes and  $30 \times 10 \times 10 \text{ mm}^3$  rectangular prisms. Layer thickness, t was set to 32  $\mu$ m for all prints, which is the  $d_{80}$  of the powder used.

Print ID	Power, $P(W)$	Scan Speed, $v$ (m/s)	Hatch spacing, $h$ ( $\mu m$ )	Volumetric energy density, VED (J/mm³)	O <sub>2</sub> level (ppm)
Cube #1	240	1.83	65	63	500
Cube #2	240	1.58	70	68	500
Cube #3	160	1.08	60	77	500
Cube #4	60	0.205	85	108	500
Cube #5	60	0.205	61	149	500
Cube #6	240	1.58	24	198	500
Prism #1	240	1.58	24	198	500
Prism #2	240	1.58	24	198	100

were found to be too severe, although the processing parameters were selected from the "Good" region on the printability map. The severity of the defects was also found to decrease with increasing VED values. It should be noted that these defects were not observed in parts printed with a less Ni-rich, i.e. Ni<sub>50.8</sub>Ti<sub>49.2</sub> (at. %) powder using the same process optimization framework in a previous study, even at lower VED values [37]. Possible reasons for the overall inferior quality of prints with the Ni<sub>51.2</sub>Ti<sub>48.8</sub> (at. %) powder of the present study will be discussed in Section 4.1. In an effort to mitigate these macroscopic defects, two more cubes (Cubes #5 and #6) were printed using the same processing parameters of the Cubes #4 and #2, but with smaller hatch spacing (h) values to reach higher VED values of 150 and 198 J/mm³, respectively. By

using this method, warping and delamination issues were dramatically reduced (Fig. 5) and Cube #6 was found to have the overall best print quality.

## 3.3. Superelasticity

Since Cube #6, fabricated at a VED value of 198 J/mm³, displayed the best print quality among other cubes, the P- $\nu$  combination used to print Cube #6 was utilized to print two rectangular prisms to be able extract dog-bone tension specimens and perform mechanical testing. The  $30 \times 10 \times 10 \text{ mm}^3$  as-printed rectangular prisms were found to be mainly austenitic microstructure under ambient conditions based on the DSC results (Fig. 6a)

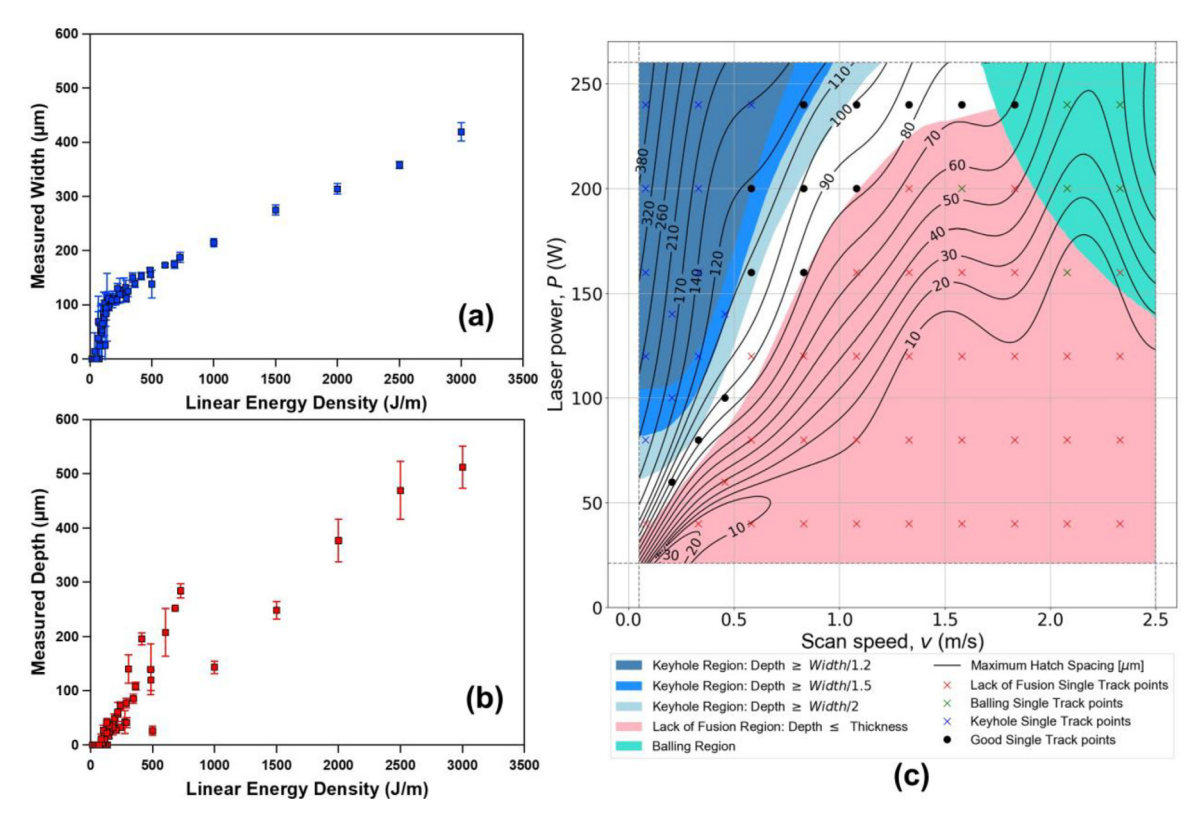


Fig. 4. Variation of melt pool measured (a) width and (b) depth as a function of linear energy density (P/v) in printed single tracks. (c) Calibrated printability map of the as-received Ni<sub>512</sub>Ti<sub>48.8</sub> (at. %) powder.

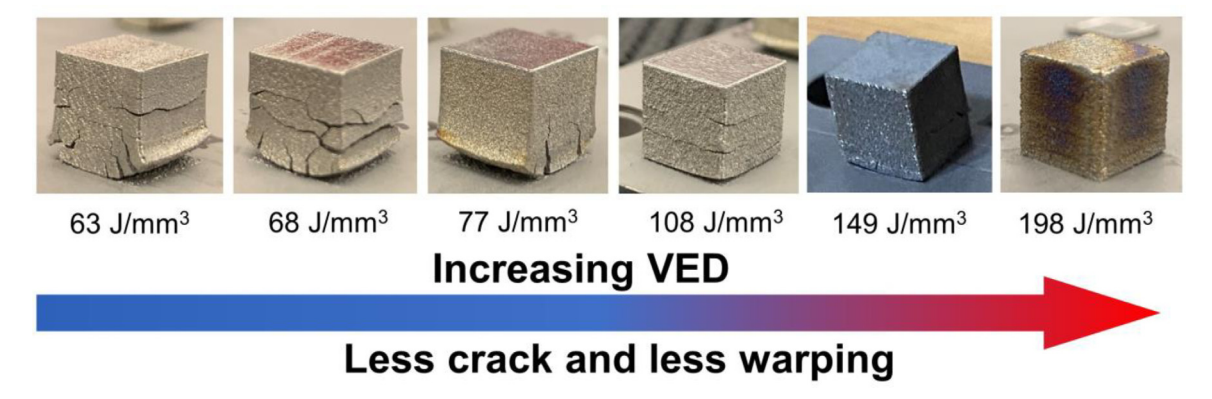


Fig. 5. As-printed cubic Ni<sub>512</sub>Ti<sub>48.8</sub> parts showing diminishing grades of macroscopic defects such as cracks, warping and delamination, with increasing volumetric energy density (VED).

with an  $A_f$  temperature  $\sim 27^{\circ}\text{C}$  (Table 2). During the incremental loading-unloading test performed both at room temperature (25°C) (Fig. 6c) and slightly above the  $A_f$  temperature (30°C) (Fig. 6e), the tensile specimen extracted from one of the as-printed rectangular prisms showed early failure. The sample exhibited very low ductility, failing at 1% without a distinct stress plateau indicative of the martensitic transformation. As evident from the oxide layer on the fabricated samples (Fig. 7), the early failure may be attributed to the severe oxidation that took place under the high VED of 198 J/mm³.

In an effort to increase the ductility of the as-printed NiTi parts,  $O_2$  level in the printer chamber was lowered from 500 ppm to 100 ppm by purging more argon through the system and another rectangular prism was fabricated using the same set of parameters. The rectangular prism printed at a 100 ppm build chamber  $O_2$  content (referred to as S100 hereafter) is noticeably less oxidized based on the colour differences when compared with the

rectangular prism fabricated under 500 ppm  $O_2$  (referred to as S500 hereafter) (Fig. 7b). Unlike S500, S100 material showed enhanced tensile superelasticity both at 25°C and 35°C (about 10°C above the  $A_f$  temperature), recovering about 4% and 6% strain, respectively. The stresses required to initiate martensitic transformation were determined as 300 MPa and 400 MPa at 25°C and 35°C, respectively. To the best of the authors' knowledge, this is the first time in SMA literature that an AM NiTi SMA reaches the end of the stress plateau during tensile loading up to 5% and continues with the elastic deformation of the detwinned martensite up to 6% strain.

Based on the stress-strain response of S100 material at different temperatures (Fig. 8a), the temperature dependence of the critical stress to induce martensitic transformation was calculated as 9.3 MPa/°C (Fig. 8b). It should be noted that the sample failed before reaching 1% strain when tested at 50°C, after undergoing 4 loading cycles to 1% strain at lower temperatures.

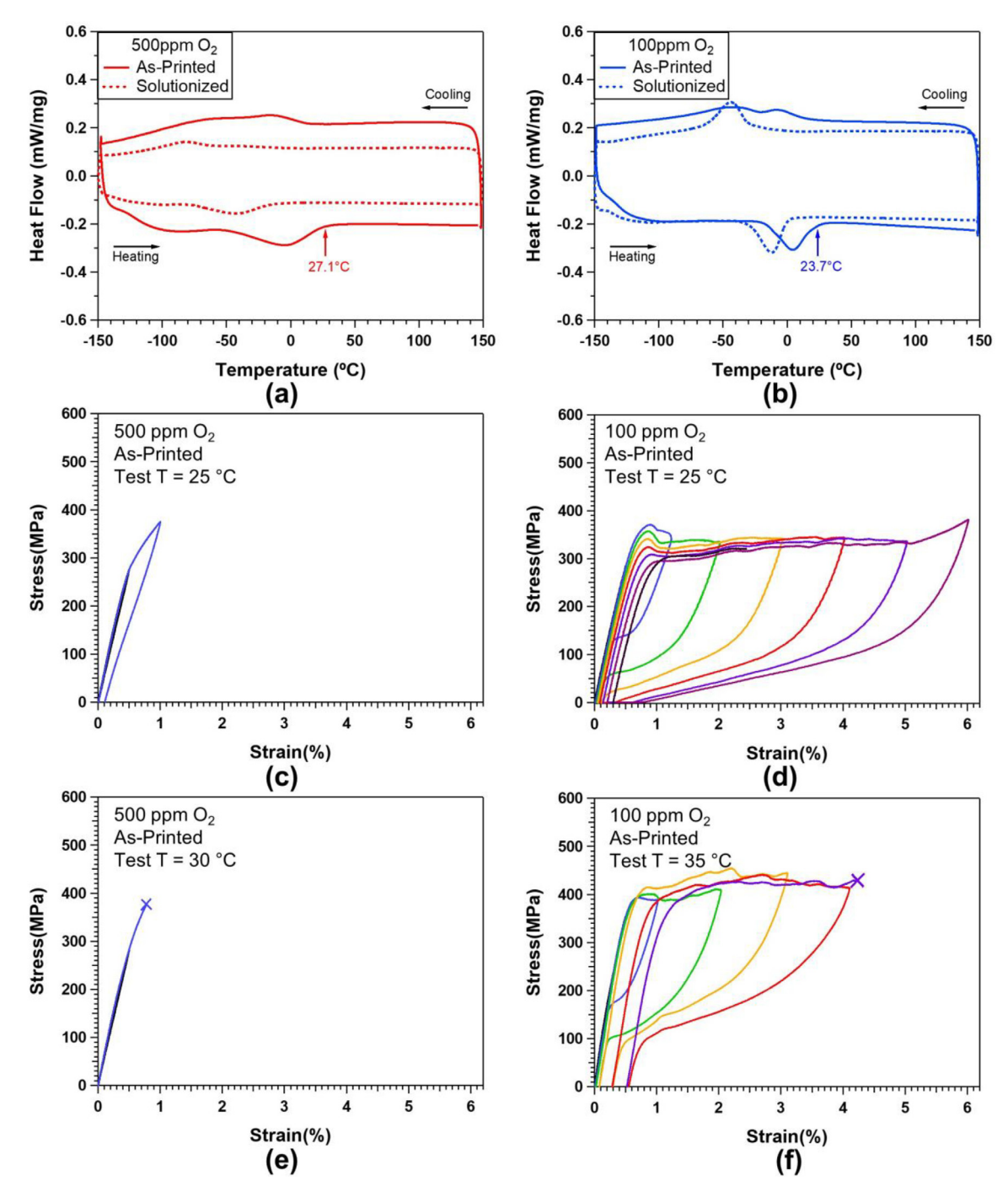


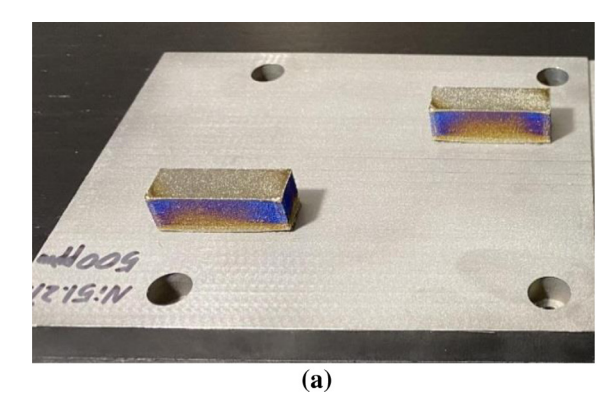
Fig. 6. DSC thermograms of  $Ni_{51.2}Ti_{48.8}$  samples extracted from rectangular prisms printed with the processing parameters ( $P_iv_ih$ ) = (240W, 1.58m/s, 24 $\mu$ m) at (a) 500 ppm and (b) 100 ppm build chamber  $O_2$  concentration. Incremental loading-unloading test results of the tensile specimens extracted from the prism printed at 500 ppm, test conducted at (c) 25°C and (e) 30°C. Incremental loading-unloading test results of the specimens extracted from the prism printed at 100 ppm, test conducted at (d) 25°C and (f) 35°C. The colors for each curve were used to distinguish different incremental loading-unloading tests.

Based on Archimedes' density analyses, the measured densities are  $6.452~g/cm^3$  and  $6.453~g/cm^3$  for \$100 and \$500 materials, respectively, which are about 99.5% of the theoretical density  $(6.4816~g/cm^3)$  of  $Ni_{51.2}Ti_{48.8}$  calculated based on an austenite lattice parameter of  $a_0=3.0127$  Å from XRD results in Section 3.4.  $Ni_{51.2}Ti_{48.8}$  nominal matrix composition was predicted from the transformation temperatures of the solutionized \$100 material (Fig. 6b) using the  $M_s$  dependence of transformation temperatures on Ni content as described in [55]. As shown in Fig. 9, the SEM images of the cross-sections parallel to the build direction also indicate that both \$100 and \$500 parts are almost

fully dense. The small number of observed pores (Fig. 9c) have diameters smaller than 10  $\mu$ m, and these pores could be a result of hollow particles in the as-received powder, that have been previously reported in NiTi powder fabricated using gas atomization [22].

## 3.4. Phase identification and crystallographic texture evolution

S100 material was found to be mainly austenitic based on room temperature XRD analyses (Fig. 10) confirming the DSC results. Low intensity peaks were detected in the samples prepared both



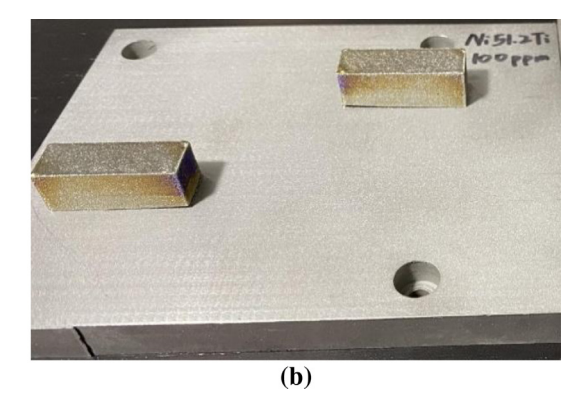


Fig. 7. a) Rectangular prisms (Prism #1) of  $Ni_{51,2}Ti_{48,8}$  samples printed with the processing parameters  $(P,v,h) = (240W, 1.58m/s, 24\mu m)$  in a build chamber with 500 ppm. b) Same processing parameters were used to print another set of prisms (Prism #2) at a build chamber  $O_2$  content of 100 ppm.

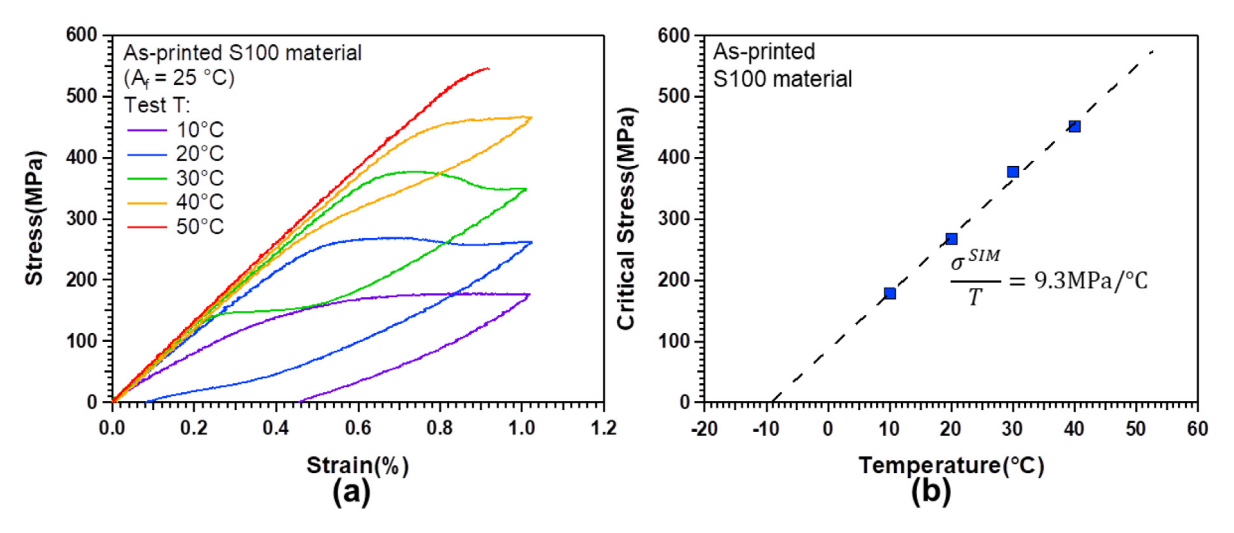
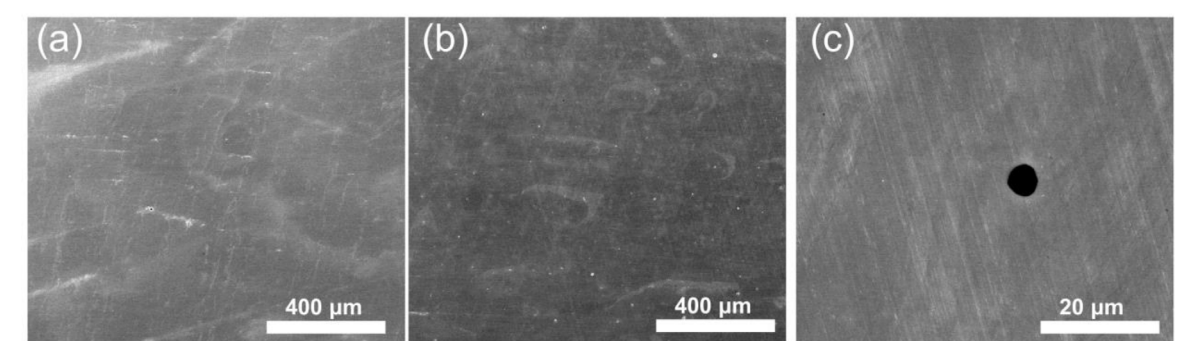


Fig. 8. a) Tensile stress-strain responses of the  $Ni_{51.2}Ti_{48.8}$  specimens printed at 100 ppm build chamber  $O_2$  concentration (S100) upon loading to 1% strain and unloading at different testing temperatures. b) Temperature dependence of the critical stress to induce martensitic transformation was determined as 9.3 MPa/°C.



**Fig. 9.** SEM images of the cross-sectional surfaces of the Ni<sub>51.2</sub>Ti<sub>48.8</sub> specimens cut parallel to the build direction in (a) S500 and (b) S100 samples. (c) A pore with a diameter less than 10 μm detected in the S100 material, possibly resulting from the hollow particles in the as-received powder.

perpendicular and parallel to the build direction as shown in the inset of Fig. 10, which indicate the presence of small amount of martensite since the transformation temperatures are very close to room temperature. However, considering the limited penetration depth of X-rays, it is anticipated that the martensite peaks may not be representative of the bulk of the sample. It is observed from peak intensities of different crystallographic planes that there is a strong texture in the as-printed part, which is actually expected and typical for AM NiTi [6]. The same texture is hypothesized to be responsible for the appearance/disappearance of martensite peaks at different angles in samples oriented parallel and perpendicular to the build direction. It is also possible to conclude that both

orientations exhibit similar internal strain levels as the locations of the major B2 peaks do not change significantly.

As a detailed texture analysis at the microstructural level, EBSD analysis was performed on the S100 samples. Fig. 11a shows an inverse pole-figure map constructed from the EBSD results for the plane perpendicular to the build direction (BD) with colors corresponding to the Z direction in the sample reference frame (IPF-Z). In this plane, a majority of the grains exhibit a <100> orientation perpendicular to the build direction (BD) in agreement with the XRD data in Fig. 10. Fig. 11b shows the IPF-Z map from a surface parallel to the BD. In agreement with the XRD results shown in Fig. 10, nearly all of the grains share a <110> orientation par-

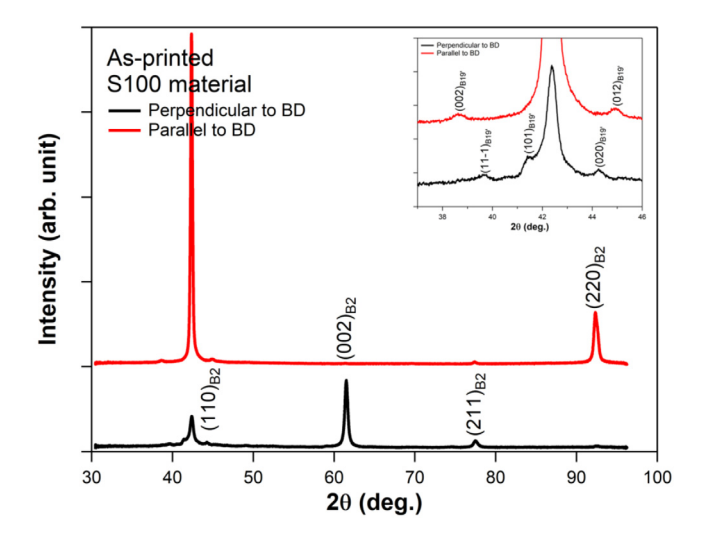


**Fig. 10.** X-ray diffraction (XRD) patterns of the  $Ni_{51.2}Ti_{48.8}$  rectangular prisms fabricated at 100 ppm build chamber  $O_2$  content. Results are for the surfaces parallel and perpendicular to the build direction (BD). The magnified pattern in the inset exihibits the low intensity peaks in detail between 38° and 46°.

allel to the BD. Formation of columnar grains along the BD is observed. The band contrast map in Fig. 11c partially reveals the melt pools, and the elongated grains extend through several melt pool boundaries. The corresponding pole figures are shown in Fig. 11d and Fig. 11e for the samples with surfaces perpendicular and parallel to the BD, respectively. It is observed that the high-angle grain boundaries are wavy and a high fraction of low-angle grain boundaries is present. Higher magnification IPF maps along with KAM maps shown in Fig. 12a and Fig. 12b, respectively, allow one to investigate the local misorientation and geometrically necessary dislocation density. They reveal the high density of sub-structures in the NiTi sample.

#### 3.5. Thermophysical properties

The specific heat capacities of the S100 and S500 materials were measured to be 0.43 and 0.44 J/g·K respectively, showing good agreement with specific heat capacity values of NiTi SMAs reported in the literature [58]. Thermal conductivity of samples is plotted against temperature in Fig. 13. In Fig. 13a, the thermal conductivity measured parallel to the build direction (with heat flux along the normal to the plane of the substrate surface) is shown

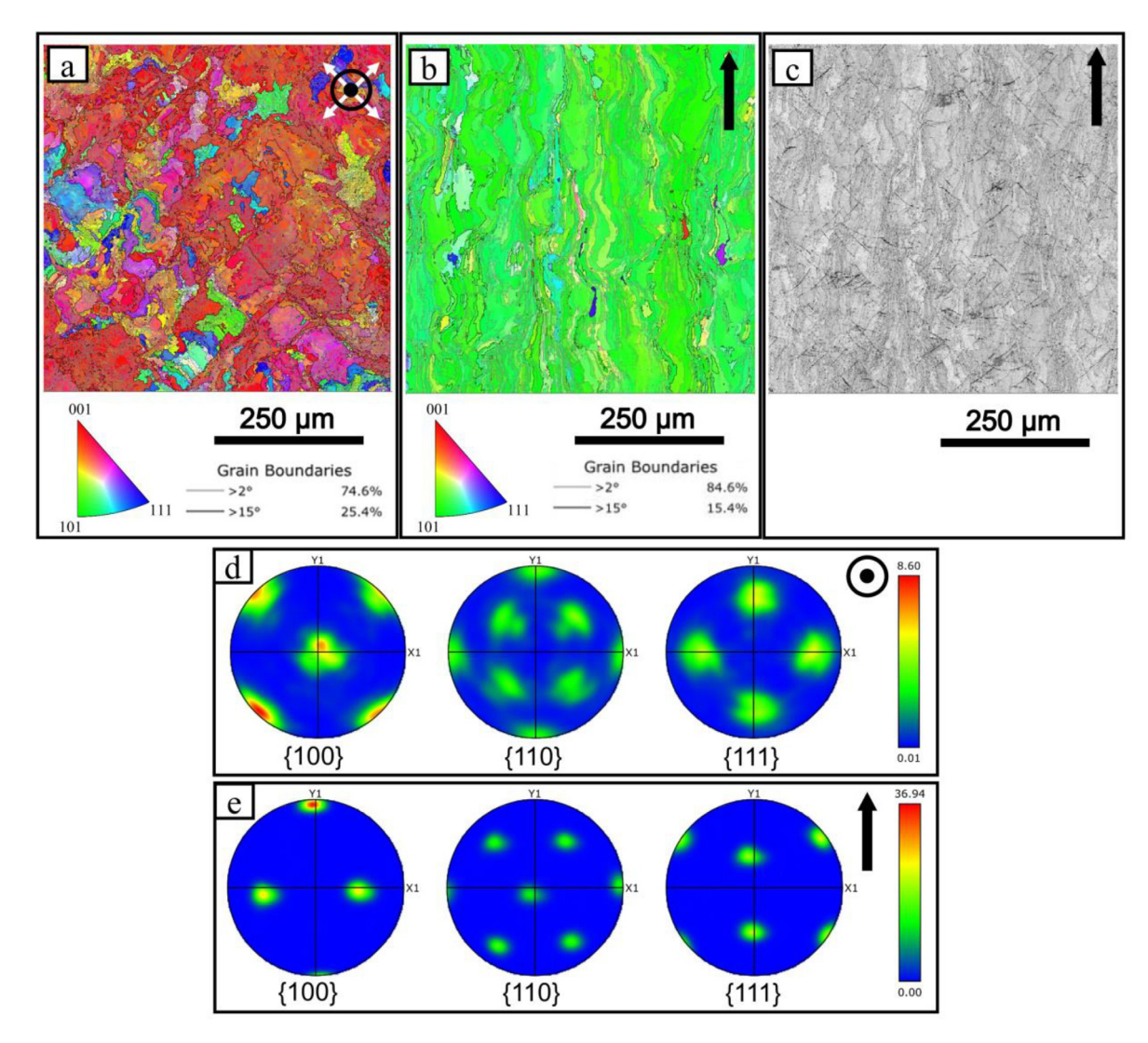


Fig. 11. Large area electron backscatter diffraction (EBSD) orientation and inverse pole figure (IPF) maps (black lines show grain boundary (GB) misalignment larger than  $15^{\circ}$  and gray lines show GB misalignment larger than  $2^{\circ}$ ) and corresponding pole figures for the cross-sections (a) (d) perpendicular and (b) (e) parallel to the build direction in the S100 samples of AM Ni<sub>51.2</sub>Ti<sub>48.8</sub>. (c) Band contrast map of the cross-section parallel to build direction partially revealing the melt pools. Black and white arrows represent the build direction and the scanning direction, respectively.

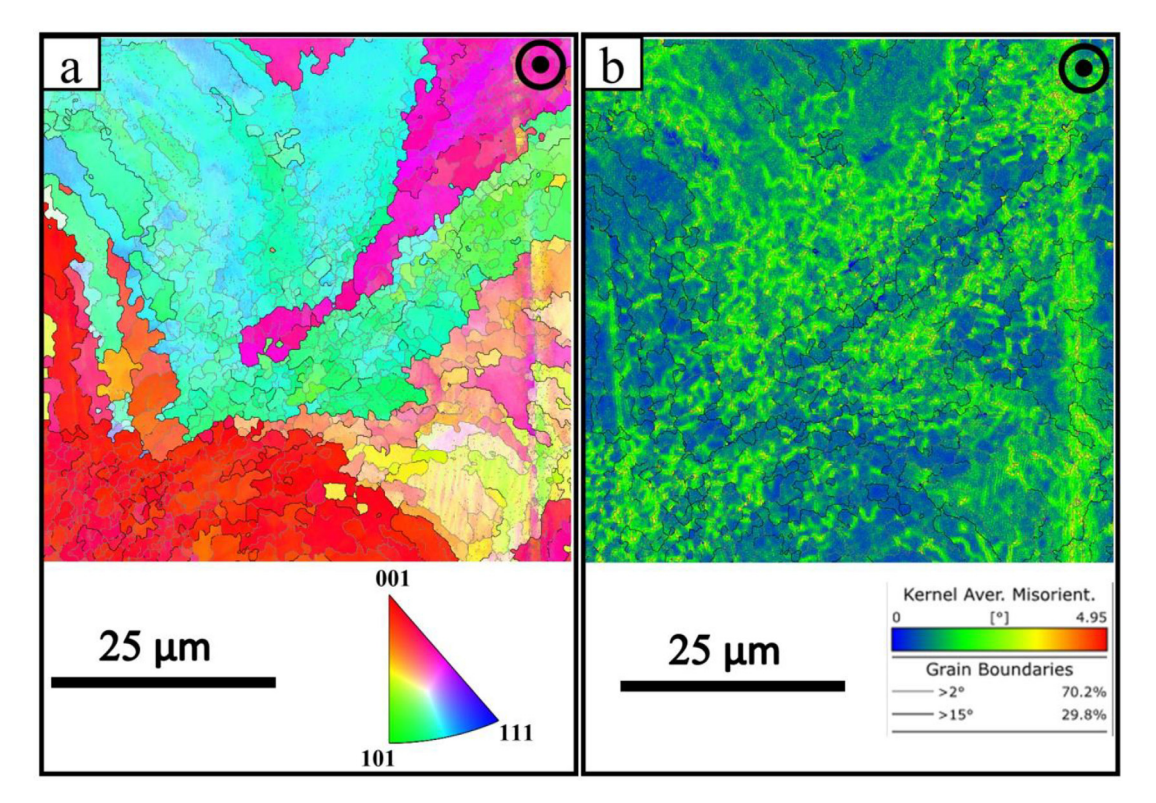


Fig. 12. (a) Small area EBSD orientation and IPF map and (b) KAM map of the S100 material of AM Ni<sub>51.2</sub>Ti<sub>48.8</sub> with the build direction out of the plane. 3 nearest neighbors are considered for the KAM map.

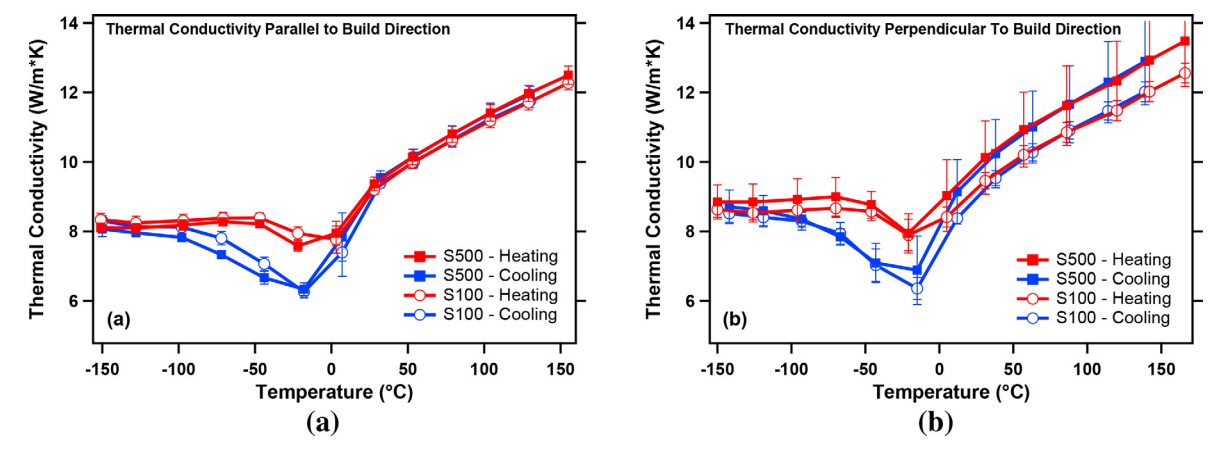
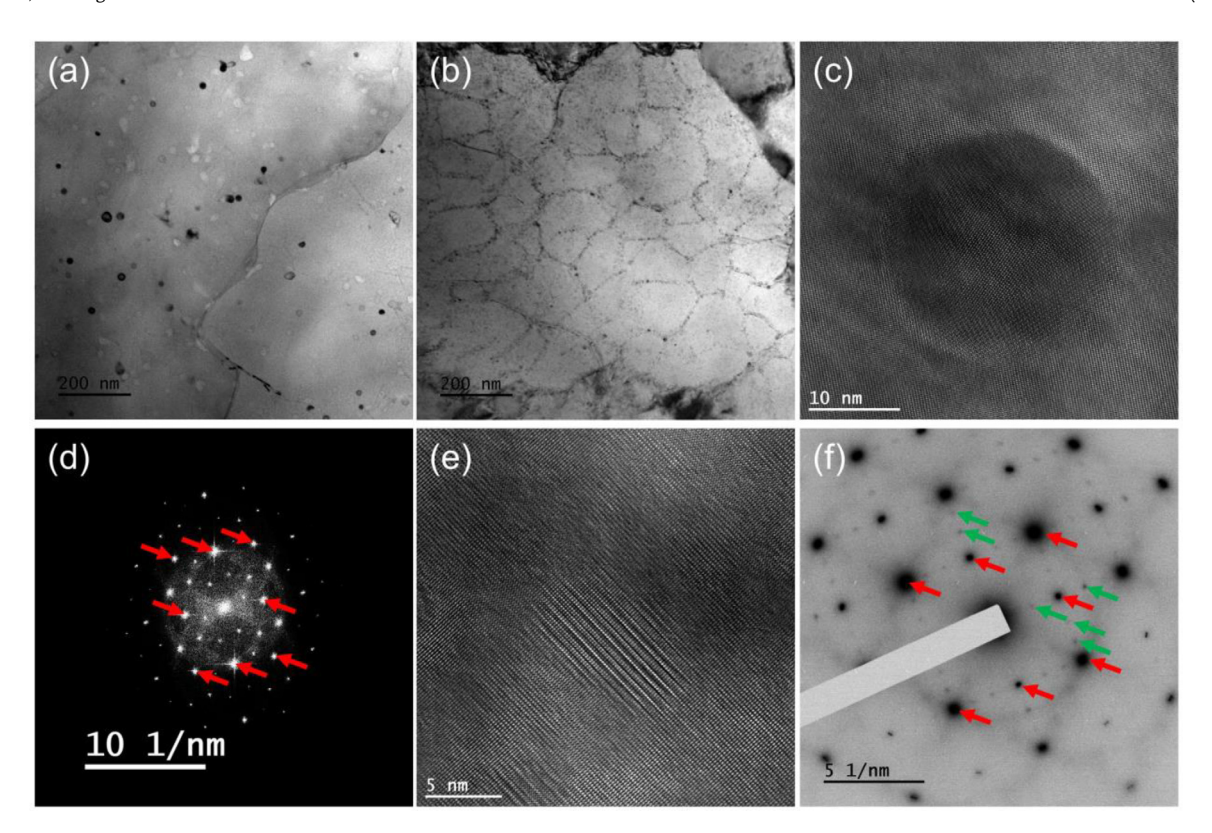


Fig. 13. Thermal conductivity of AM  $Ni_{51,2}Ti_{48.8}$  measured (a) parallel to the build direction and (b) perpendicular to the build direction. Measurements taken from S100 material are represented by the circular markers, and those taken from S500 material are represented by the square markers. The error bars correspond to one standard deviation above and below the average value.

for both the S100 (open circles) and S500 (solid squares) samples. Each data point represents the average of the thermal conductivities measured in seven samples taken from varying heights within the as built prisms. Although there was some scatter among the thermal conductivities measured at different build heights (indicated by the 1-standard deviation error bars) there was no trend with respect to build height in either the S100 or S500 samples. Furthermore, there was little difference in thermal conductivity between the S100 and S500 samples as indicated by the proximity of the corresponding curves in Fig. 13a. In Fig. 13b, the thermal conductivity measured perpendicular to the build direction (with heat flux direction within the plane of the build plate surface) is plotted against temperature for the S100 and S500 samples, where each data point represents the average thermal conductivity measured in three samples. Although the average thermal conductivity

of the S100 samples is lower than that of the S500 samples, significant spread in the S500 data suggests that the difference may not be statistically significant, as shown by the overlapping error bars between the two curves. In order to determine whether the measurement direction or build chamber  $O_2$  level have a statistically significant effect on the thermal conductivity of the printed material, t-tests were performed on the 55°C data points using 95% confidence intervals (significance level  $\alpha=0.05$ ). In each case, the resulting p-value was greater than the significance level, indicating that the observed differences in thermal conductivity are not statistically significant. Therefore, it cannot be concluded that build chamber  $O_2$  level or measurement direction has an effect on the thermal conductivity.

Regardless of measurement direction and build chamber  $O_2$  level, the thermal conductivity curves show similar behaviour with



**Fig. 14.** TEM micrographs representative of the distribution and structure of secondary phases in the S500 samples of AM Ni<sub>51.2</sub>Ti<sub>48.8</sub>. (a) A bright Field (BF)-TEM image showing region with randomly distributed, spherical particles. (b) Another BF-TEM image showing region with networked, non-uniformly shaped particles. (c) Absolute background filtered HRTEM showing a spherical particle. (d) FFT of (c) with [110]-oriented NiTi austenite matrix reflections indicated by red arrows. (e) Absolute background filtered HRTEM showing a coherent particle representative of the networked particles shown in (b). f) The selected area electron diffraction (SAED) image from an area with networked particles with [100]-oriented NiTi austenite matrix reflections indicated by red arrows and secondary phase reflections indicated by green arrows.

changing temperature. Upon heating from -150°C, thermal conductivity increases slightly and subsequently dips during reverse martensitic transformation. The austenite phase shows higher thermal conductivity as well as increased sensitivity to temperature increase compared to the martensite phase. As the samples were cooled down through martensitic transformation, thermal conductivity dipped significantly lower than during the reverse transformation. The thermal conductivities in both the martensite and austenite phases are lower compared to the thermal conductivity measured in bulk  $Ni_{50}Ti_{50}$  [59]. At temperatures of -100°C and 100°C representing the martensite and austenite phases respectively, bulk Ni50Ti50 showed thermal conductivities of approximately 12 and 16 W/m·K [59], whereas the AM Ni-rich NiTi of the present study showed average thermal conductivities of approximately 8.5 and 11.5 W/m·K. This difference in thermal conductivity may be attributed to the differing composition and the unique microstructure of AM NiTi with increased number of defect sources, e.g. non-metallic inclusions, precipitates and increased dislocation density, acting as phonon scattering centers. Further investigation is needed to isolate the effects of compositional and microstructural effects on the thermal conductivity of AM NiTi SMAs.

### 3.6. Transmission electron microscopy (TEM)

As shown with superelastic testing results in Fig. 6, S100 material exhibited enhanced superelasticity, with the highest recoverable strain recorded in literature so far. On the other hand, S500 material failed in a brittle manner without showing any sign of superelasticity. TEM was performed to reveal the role of microstructural features, especially the presence of different types of non-metallic inclusions and precipitates, on the observed differences in the mechanical behavior of the as-printed NiTi samples.

TEM imaging revealed that both the S500 (Fig. 14) and S100 (Fig. 16) materials have qualitatively similar microstructures consisting of highly irregular grains with curved, wavy grain boundaries and a large amount of low angle grain boundaries. In addition, both conditions had a very high density of secondary phase particles. The microstructure of the S500 sample was inhomogeneous, with the distinct distributions of secondary particles varying from one area to the next. As shown in Fig. 14a there were regions of the specimen containing 20-50 nm spherical particles that had no clear preferred orientation relative to the surrounding matrix. The background filtered high resolution TEM (HRTEM) image and corresponding fast Fourier transform (FFT) shown in Fig. 14c and Fig. 14d are representative of these particles.

In addition, there were large regions of the S500 sample that contained networks of < 20 nm particles that appeared similar to subgrain networks, as shown in Fig. 14b. The HRTEM and selected area electron diffraction (SAED) shown in Fig. 14e and Fig. 14f reveal a clear orientation relationship between these particles and the matrix. However, the d-spacings observed do not match well with any of the known secondary phases in NiTi including pure and mixed oxides. STEM - High-angle annular darkfield imaging (HAADF) and STEM-EDS (Fig. 15) indicate that both types of particles contain oxygen and are poor in Ni relative to the matrix.

Similar to the S500 samples, the S100 samples also contained two distinct distributions of secondary phase particles. As shown in Fig. 16a and Fig. 16b, some areas of the samples contained randomly distributed spherical particles, while other regions showed a network of particles. HRTEM revealed that there were very fine (<15 nm), randomly distributed coherent particles present in addition to the larger particles shown in Fig. 16a. A representative particle and the corresponding FFT are shown in Fig. 16c and Fig. 16d,

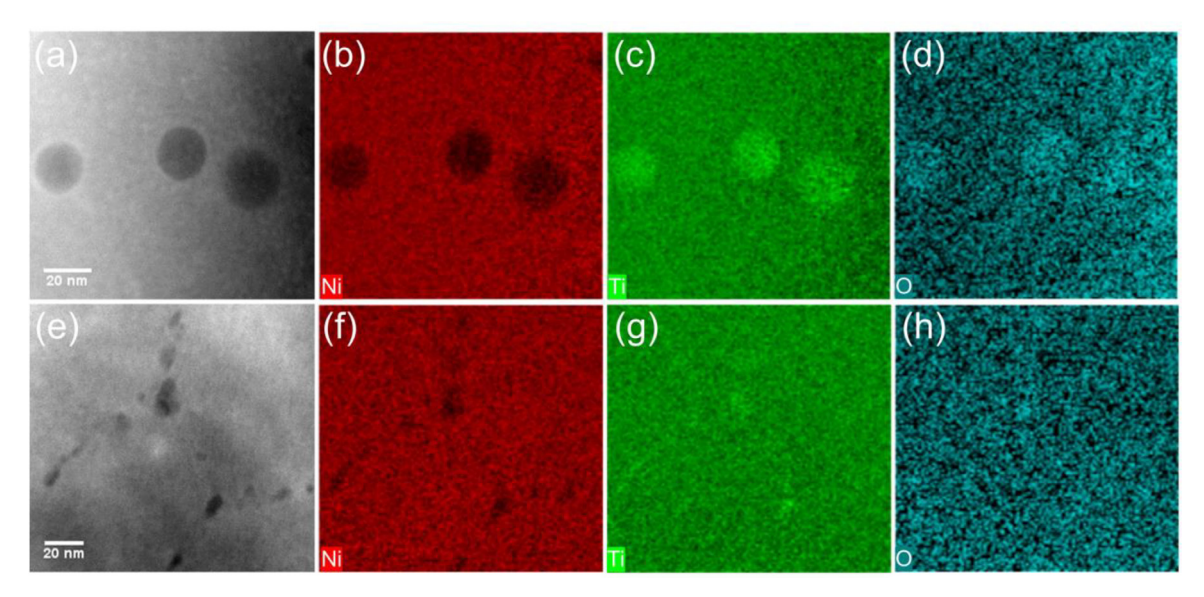
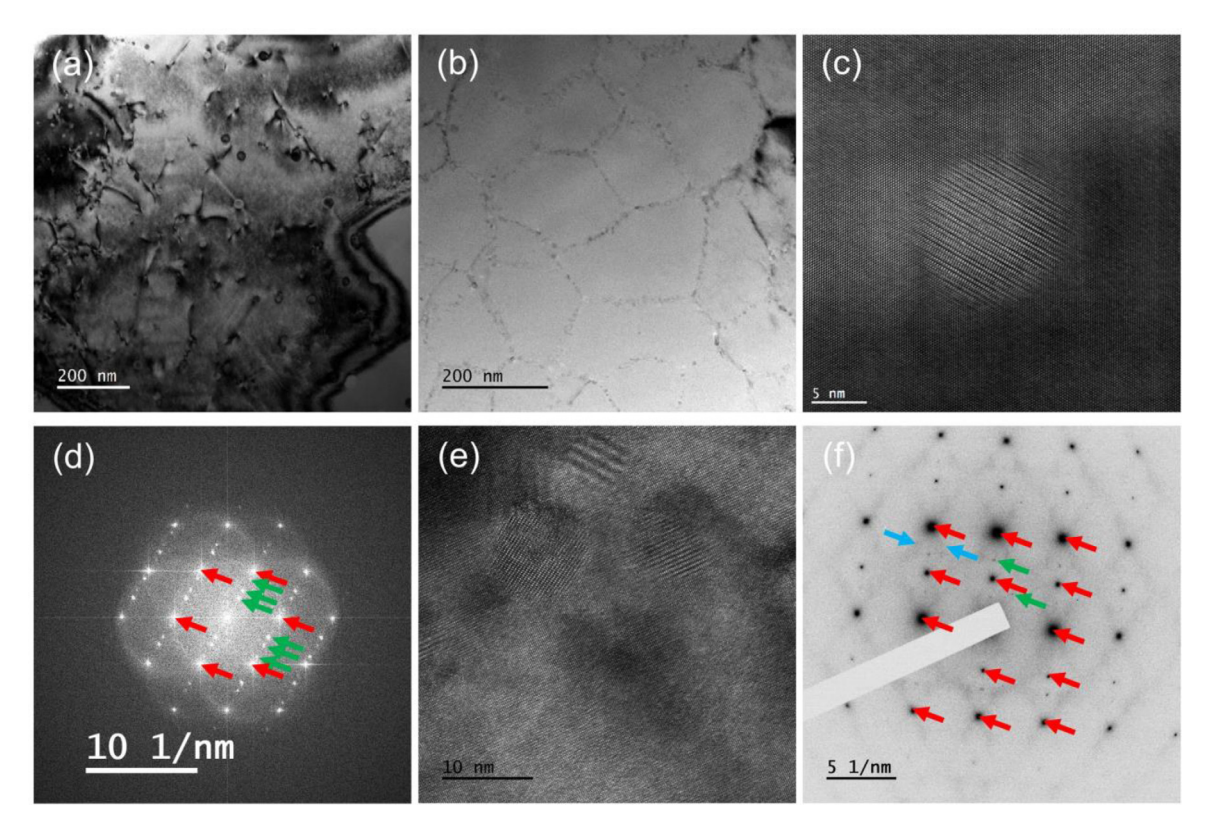


Fig. 15. STEM-HAADF and EDS maps of (a-d) spherical secondary phase particles and (e-h) networked particles in the S500 samples of AM Ni<sub>51.2</sub>Ti<sub>48.8</sub>. (a & e) HAADF images with brightness proportional to atomic mass. (b & f) at.% Ni maps. (c & g) at.% Ti maps. (d & h) at.% O maps.



**Fig. 16.** TEM micrographs representative of the distribution and structure of secondary phases in the S100 samples of AM  $Ni_{51.2}Ti_{48.8}$ . (a) A BF-TEM image showing region with randomly distributed, spherical particles. (b) Another BF-TEM image showing region with networked, non-uniformly shaped particles. (c) Absolute background filtered HRTEM image showing a 14 nm diameter, coherent particle. (d) FFT of (c) with [111]-oriented NiTi austenite matrix reflections indicated by red arrows and secondary phase reflections indicated by green arrows. (e) Another HRTEM image showing several particles of different orientations representative of the networked particles shown in (b). (f) SAED from an area with networked particles with [110]-oriented NiTi austenite matrix reflections indicated by red arrows and secondary phase reflections indicated by green arrows highlight streaking observed in the pattern indicating a potential range of lattice parameters in the secondary phase particles present.

respectively. The d-spacings observed in Fig. 16d do not match well with any of the expected secondary phases, but HAADF imaging of this region indicates that these nm-scale precipitates are Ni-rich, as shown in the STEM-HAADF image in Fig. 17a. Unlike in the S500 sample, as shown in Fig. 16e and Fig. 16f, the networked particles do not have a clear preferred orientation. As shown in Fig. 17, STEM-HAADF and STEM-EDS confirm that both the networked par-

ticles and the larger, spherical particles are Ti-rich oxides, similar to what was observed in the S500 sample.

While it is difficult to quantify the particle density due to the unknown thickness of the samples and the variation in visibility of particles due the various orientations present, the line-intercept method was used to determine the network spacing in both conditions. The mean network spacing for the S500 samples were 104.1

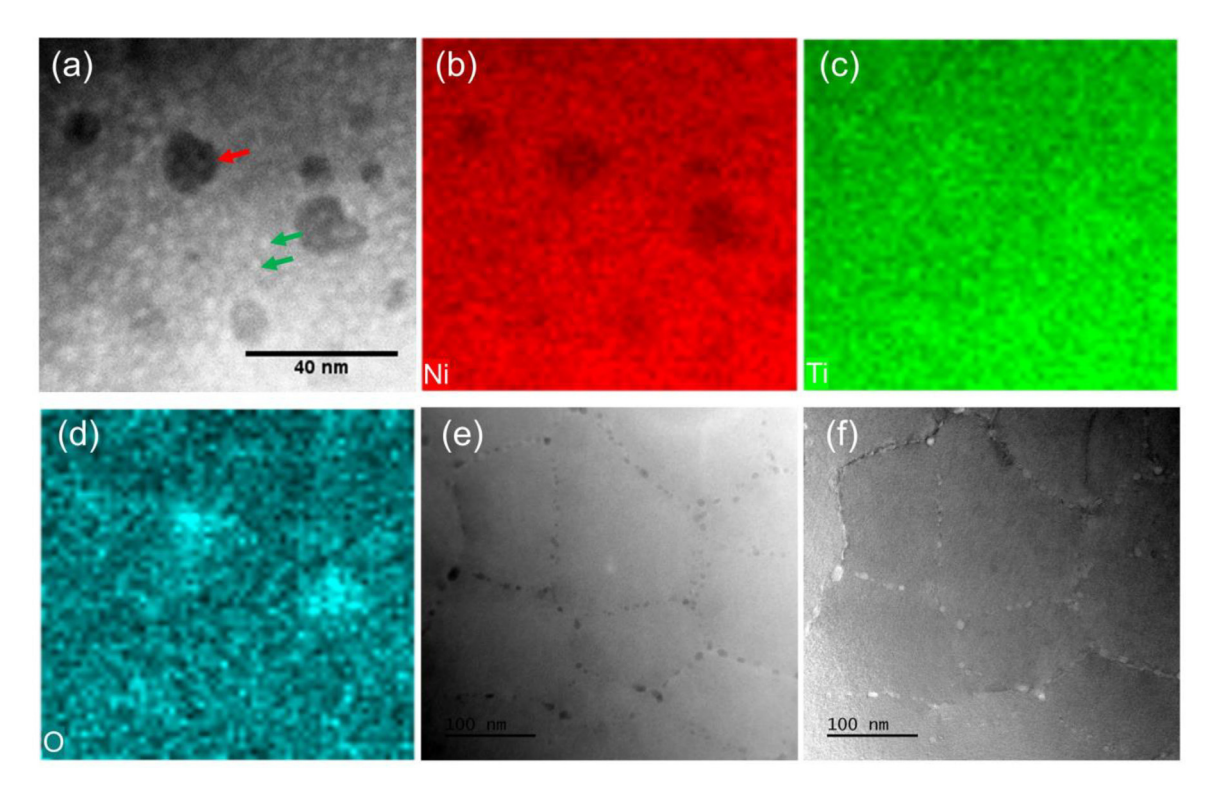


**Fig. 17.** STEM images and EDS maps showing secondary phase particles in the S100 samples of AM Ni<sub>51.2</sub>Ti<sub>48.8</sub>. (a) A HAADF image showing larger, Ni-poor oxide particles like the one indicated by the red arrow and smaller, Ni-rich particles like those indicated by the green arrows. (b) at.% Ni map corresponding to (a). (c) at.% Ti map. (d) at.% O map. (e) A HAADF image of the region containing networked, Ni-poor oxide particles. (f) The STEM-BF image of the region shown in (e).

nm, whereas for the S100 samples it was 127.6 nm, indicating a higher volume of oxide particles in the S500 samples.

## 4. Discussion of the Results

## 4.1. Fabrication of defect-free NiTi SMA parts

Processing parameters P and v were systematically varied based on a previously developed process-optimization framework [37, 51, 57] and h was selected based on a maximum hatch spacing criterion for the fabrication of defect-free parts from a Ni-rich NiTi SMA powder feedstock [37]. 66 single tracks were printed to be able to select the optimal single track parameters that will yield a continuous melt pool with desired depth and ideally avoid porosity resulting from keyholing, lack of fusion and balling phenomena. It is well known that the selection of a sufficiently small h can ensure the overlap and remelting of the adjacent tracks, while energy input, i.e. the volumetric energy density (VED), controls the extent of Ni evaporation from the molten powder [37], hence the transformation temperatures of the printed part. As illustrated in Fig. 4, optimal P-v combinations based on single tracks along with h values determined from the maximum hatch spacing criterion was not able to avoid the macroscopic cracks in the printed parts and their delamination from the build surface of the substrate. It is possible that these defects stem from the high Ni content of the starting powder since, as mentioned previously, none of these defects were encountered when a less Ni-rich powder was used in a previous study [37]. However, in the same study, only partial superelasticity could be obtained in the printed parts due to the lack of strengthening mechanisms such as coherent Ni-rich precipitates and solid solution hardening from higher Ni contents. Therefore, a more Ni-rich powder was selected with the aim of forming Ni-rich precipitates and taking advantage of higher Ni contents towards solid solution hardening to strengthen the matrix and ultimately achieve superior superelasticity in the printed parts with a large recoverable strain. Smaller h values were utilized to increase VED and evaporate just enough Ni to achieve superelasticity near room temperature and to suppress macroscopic defects. It was shown that the cracks and delamination from the substrate were noticeably mitigated at higher VED values (Fig. 5). Listed below are the possible reasons that the as-printed parts were not able to be fabricated defect-free without a necessary reduction in h values:

- a The gas atomization method used to fabricate the specific powder feedstock used in this study was reported to have notable internal pores within the powder particles [60] and this explains some spherical porosity observed in the final NiTi prints. Additionally, carbon contamination from the graphite crucible during the gas atomization process may limit the ductility and make the prints more prone to cracks and delamination.
- b The bidirectional scanning pattern with a 45° angle employed in this study may generate a large thermal gradient during printing and result in excessive residual stress [61, 62] within the NiTi parts.
- c At low VED values, the resulting matrix is more Ni-rich with the chances of precipitating out strengthening second phases and ending up with increased strength at the expense of ductility. In addition, it is well known for NiTi SMAs that the higher the Ni content, more brittle the material becomes [63]. The initiation of cracks from defects like pores or inclusions will most likely be easier, especially in the presence of residual stresses.
- d Increasing transformation temperatures were observed with increasing VED due to increased Ni evaporation, similar to the results presented in [37]. Even if the transformation temperatures of the parts printed at high VED values were slightly below room temperature, each layer of these parts may be able to transform back to the martensite under potentially graded residual stress during cooling and before the subsequent layer is printed. Martensitic transformation may help the relaxation

of the residual stress introduced by the thermal gradient during the laser melting process. In contrast, in the absence of martensitic transformation, e.g. in parts built with lower VED values, residual stresses might cause cracks, warping and delamination problems.

O<sub>2</sub> level in the build chamber was shown to be critical for controlling the high temperature oxidation during the printing process, especially at elevated VED levels. O2 control has already been reported to be critical for the mechanical properties for AM NiTi and a lower chamber atmosphere O2 content of 25 ppm, which is much lower than the 500 ppm required by ASTM F2063-05, was suggested by Wang et. al. [20] for improved tensile ductility. In the current study, tensile ductility was shown to dramatically increase and superelastic recovery could be achieved by solely decreasing the O<sub>2</sub> level in the chamber from 500 ppm to 100 ppm. TEM observations revealed that the size and volume fraction of oxide particles were smaller in parts built at a chamber O2 content of 100 ppm compared to 500 ppm. Hence was the necessity to limit the chamber O2 content at high VED levels for improved ductility. Depending on the capability of different L-PBF systems, O2 content may be decreased even further, e.g. as low as 25 ppm as shown in the work of Wang et al. [20].

At high VEDs, not just the oxidation but also the residual stresses are expected to be higher due to larger thermal gradients inside the printed part. Warping may accumulate during the layer-by-layer building process under the residual stress, but the resulting strains may be accommodated via the martensitic transformation as discussed above. It is also likely that high VEDs increase the temperature of the currently printed layer and may help relieve the residual stresses stored in the previously built layers. As an alternative to increasing VED through a decrease in h values, it may also be possible to eliminate cracks and delamination in Nirich NiTi through using a more complex scanning pattern than the  $45^{\circ}$  bidirectional pattern used in the present study or employing a pre-heated substrate that will result in smaller thermal gradients.

It should be noted that the determination of the "good" printable region in the printability map in Fig. 4c is, to some extent, conservative. During printing, the temperature of the region in the vicinity of the current single track may increase due to thermal conduction, and the energy required to form a melt pool with a given depth might decrease. Therefore, the minimum requirement of d>t (layer thickness) may be slightly relaxed and it is indeed possible that fully dense NiTi parts can be fabricated in the "lack of fusion" region that is close to its upper boundary near the "good" printable region, especially with the selection of smaller hatch spacing values.

## 4.2. Tailoring the transformation temperatures in AM NiTi

Unlike the conventional fabrication methods typically used for the fabrication of NiTi, e.g. vacuum induction melting, oxygen pickup during the layer-by-layer fabrication in L-PBF processes is much more critical as each of the many layers that comprise the part is prone to oxidation during printing depending on the atmospheric cleanliness of the printer chamber. Therefore, in addition to Ni evaporation, possible precipitation reactions and the unique AM defect structure as a result of rapid cooling, oxidation may also play a role in the evolution of transformation temperatures of AM NiTi based on different types of oxide particles observed in the TEM study. As most of these oxides, if not all, are Ti-rich due to the higher affinity of Ti towards oxygen, Ti is depleted from the matrix, tending to decrease the transformation temperatures at relatively higher VED values, countering the effect of Ni evaporation. The solutionized  $Ni_{51.2}Ti_{48.8}$  (at. %) powder showed no sign of martensitic transformation within a temperature range of -150°C to  $150^{\circ}$ C (Fig. 3d). During printing of rectangular prisms, the evaporation of Ni with the selection of appropriate processing parameters resulted in the appearance of transformation peaks within the same temperature range (Figs. 6a and 6b). When the DSC results of the solutionized rectangular prisms printed at 100 and 500 ppm  $O_2$  are compared, it is observed that \$100 material exhibits slightly higher transformation temperatures. This correlates well with the assumption that increased oxidation leeches more Ti from the matrix, decreasing the transformation temperatures and TEM images in Section 3.6 indeed show a qualitative trend of increased area fraction and size of the oxide particles.

#### 4.3. Crystallographic texture evolution and its effect on superelasticity

Crystallographic texture of the S100 material has been investigated and a strong <110> orientation has been observed along the loading axis of the dog-bone tension specimens extracted from the rectangular prisms (Fig. 11e). Another notable observation is the formation of near pseudo single crystals in the printed NiTi samples (Fig. 11). Due to the epitaxial growth in the layer-by-layer fabrication process, the columnar grains with similar orientations form a microstructure resembling a single crystal. In this section, we will discuss the effects of the process parameters selected here, in particular the linear energy density (LED) which changes the melt pool shape, hatch spacing, and rotation angle of the laser tracks between the successive layers, on these two observed phenomena.

In the S100 samples, the [001] direction is aligned parallel to the build direction whereas the [100] and [010] directions are aligned parallel/perpendicular to the laser scanning directions (Fig. 11d, Fig. 11e, Fig. 18a and Fig. 18b). This texture and the loading direction of the tensile samples are some of the reasons why good tensile superelasticity was achieved in these samples, which is better than what is reported in the literature so far. It is well known that texture plays a major role on the thermomechanical response of NiTi SMAs. Gall et al. [41, 64, 65] have reported the mechanical properties of Ni-rich NiTi single crystals tested along different crystallographic orientations. The single crystals with <001> orientation along the loading axis exhibit higher critical stresses to induce martensitic transformation during tensile testing and premature fracture (at <2% strain), while the <110> orientations result in a high recoverable strains (>5%) with the martensitic transformation triggered at relatively lower tensile stresses (under the same aging conditions and test temperatures). Considering the premature fracture of the NiTi single crystals along the <001> orientation in tension [64, 65], the AM NiTi parts, especially the ones with higher Ni contents than equiatomic composition, should not have a strong <001> texture along the tensile axis for good superelastic performance.

The <001> direction is the fastest crystal growth direction [66] along the highest thermal gradient during solidification of cubic materials, and the <001> growth textures have been reported in AM NiTi samples [6, 31, 43]. At first glance, the <001> texture along the build direction may seem to result from the high thermal gradient between the molten layer and the substrate or the previously printed layer (Fig. 18c). However, considering the melting and solidification processes during the laser scanning process, there is also a large thermal gradient between the current laser track and the adjacent previously solidified track. For example, it has been reported that hatch spacing (h) between the laser tracks affects crystallographic texture strength, smaller h values induce stronger textures in AM NiTi by increasing the number of remelting and solidification cycles, hence favouring the grain growth (forming pseudo single crystal structure) and better alignment of <001> orientation with the build direction [31, 36]. However, <011> orientation along the build direction has been re-

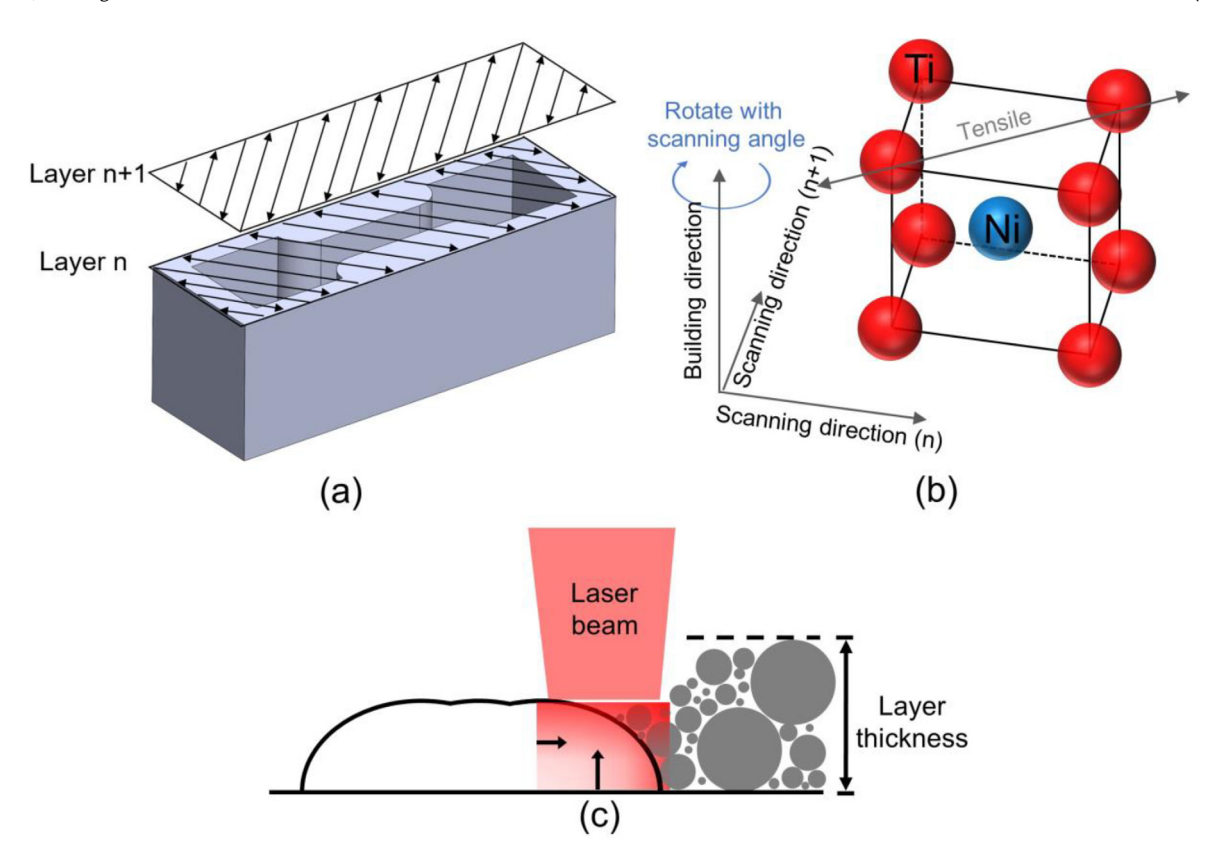


Fig. 18. Schematic drawings of (a) scanning patterns and tensile specimen orientation in the AM Ni<sub>51,2</sub>Ti<sub>48,8</sub> rectangular prisms in the present study, (b) B2 austenite lattice orientation with respect to the build direction and scanning directions in the AM samples based on the measured texture in Fig. 11, (c) thermal gradient directions in the molten layer during the laser scan.

ported in some other AM cubic materials (e.g., 316L stainless steel [67–69]) by using a rotation angle of 0° or 180° between the successive layers. Therefore, it is important to understand the underlying mechanisms of texture evolution during AM processes and utilize it as guidance to achieve desired textures in SMAs in order to accomplish near perfect superelasticity along different directions of the built parts. Yet, the texture studies on AM NiTi SMAs are limited [31, 36, 43, 70]. This is because of the difficulty of measuring the austenite texture (which is the relevant texture for the superelastic behavior) above room temperature which necessitates studying Ni-rich compositions with the austenite phase at room temperature. In addition, many of the earlier AM NiTi works were not able to achieve pseudo single crystals in Ni-rich NiTi compositions.

# 4.3.1. Effects of laser power and scan speed on crystallographic texture evolution

The shape of the melt pool may play an important role in the texture evolution during AM as it affects the direction of the local thermal gradient. As previously demonstrated with single track prints in Section 3.2, the melt pool geometry can change from a keyhole mode (Fig. 19a) under a relatively high LED value (thus, high laser power or low scan speed) to a shallow shape (Fig. 19b and Fig. 19c) under low LED values. At low LED values, the melt pool has a flatter bottom and is more likely to develop a <001> texture along the build direction as the thermal gradient is larger along the build direction. In our process optimization framework, the "good" tracks are defined conservatively with the criteria of d< w/2 for avoiding possible keyholing porosity (Fig. 4c) and thus, they are likely to result in the development of <001> texture along the build direction.

Sun et al. [69] have reported that <011> orientation was aligned with the build direction in AM 316L steel. Their melt pool shape (as a result of the high LED values they used) can be defined as the keyhole type based on the process optimization framework presented above. Fig. 19a schematically illustrates the melt pool shapes that Sun et. al. [69] observed when they achieved <011> texture along the build direction. This schematic also explains the mechanism proposed to rationalize the growth of <001> oriented grains 45° to the build direction due to the highest local thermal gradient direction perpendicular to the solid-liquid interfaces of the keyhole melt pools shown in the schematic. Fig. 19b and Fig. 19c also illustrate potential texture evolution mechanisms for low LED melt pool shapes. In short, Fig. 19 explains a potential mechanism to control the texture during AM process based on the melt pool shapes through the control of LED value, and thus, laser power and scan speed.

## 4.3.2. Effects of hatch spacing on crystallographic texture evolution

The value of h may also affect the texture in AM NiTi parts. Andreau et al. [67] proposed a mechanism for forming <011> texture along the build direction in 316L steel taking the effect of h into account. Based on this mechanism, the epitaxial growth at the overlap of the molten region with the previously printed track will favour the crystallographic orientation that has less misalignment for lowering the nucleation energy of new nuclei, and the growth direction may have a small angular difference with the local thermal gradient (Fig. 19b). As printing takes place, this orientation will gradually dominate the others. However, h used in our NiTi parts is very small (24  $\mu$ m, a quarter of the melt pool width, Fig. 19c), so the epitaxial growth can start from a flatter region in the mid-bottom of the melt pool. At the mid-bottom region of the previously (or the first) printed track will have a <001> orienta-

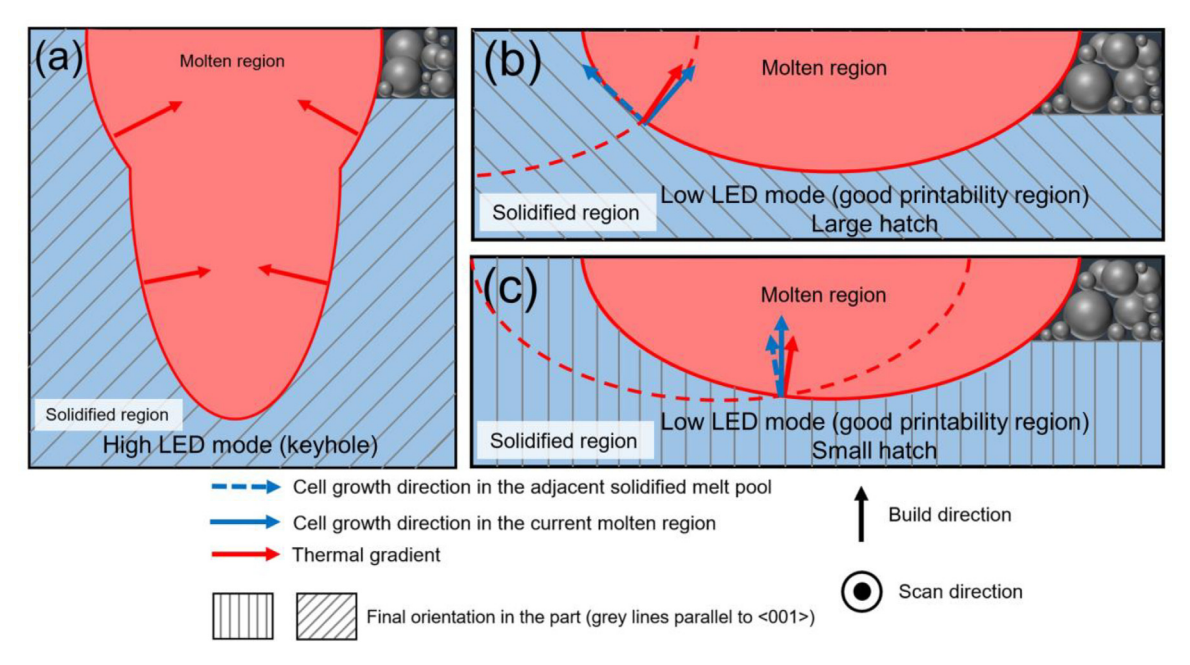


**Fig. 19.** Schematic illustration depicting the thermal gradient and solidification direction under (a) high linear energy density (LED) (keyholing mode) [69], (b) lower LED (good print region in Fig. 4c) with large hatch spacing, and (c) lower LED (good print region) with small hatch spacing as used in the present study. The melt pool becomes shallower and flatter under lower LED, so the thermal gradient and solidification direction are mostly along the build direction in the present case with small hatch spacing, which results in the <001> texture formation in (c). Cell growth direction from the solid-liquid interface indicates <001> orientation formation since it is the fastest crystal growth direction for cubic materials. The schematics were constructed for the rotation angle cases of 0° or 180° between the successive layers.

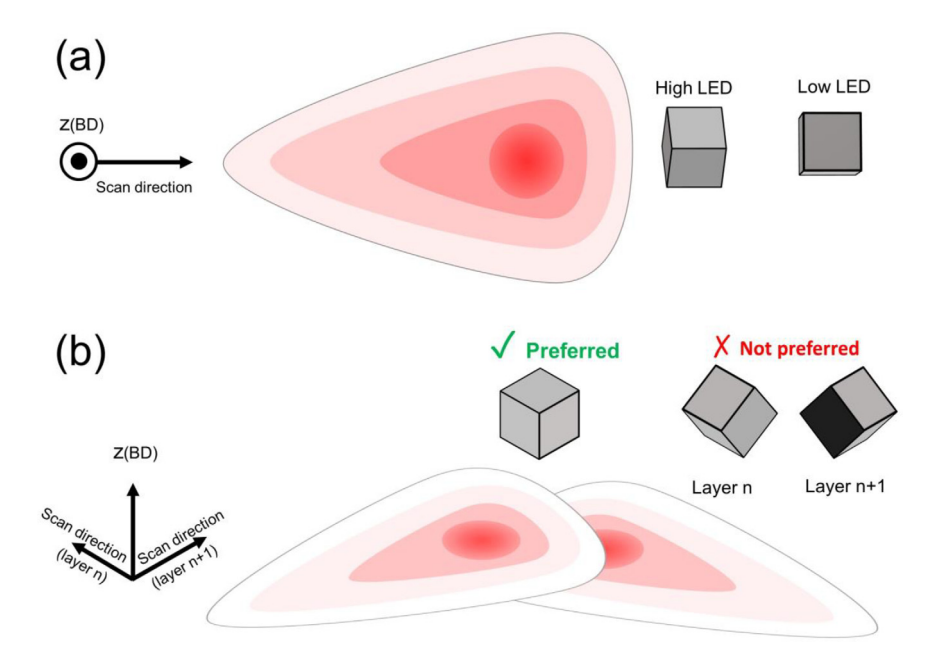


**Fig. 20.** Schematic of the orientation selection/growth mechanism during (a) single-layer scanning (lattice cells were slightly rotated for better view) and (b) multi-layer scanning with a 90° rotation angle of scan directions. Both orientations would be possible for single-layer, but only the <001> would be favoured due to its less misalignment with the previous sintered layer for the multi-layer situation.

tion along the build direction, which is aligned with the thermal gradient during its solidification. As more tracks are printed, this orientation may be inherited and dominate others.

4.3.3. Effects of rotation angle between successive print layers on the crystallographic texture evolution

The rotation angle of the scan directions between successive layers may also influence the resulting texture. As shown in

Fig. 20a, both <001> and <011> orientations along the build direction could be possible during a single layer scan depending on the melt pool shape and h value, as described in Fig. 19 . However, if a rotation angle of  $90^\circ$  is imposed between layers (Fig. 20b), the <001> orientation would be preferred along the build direction since this orientation would perfectly match between the layers and have minimum misalignment. In addition, this orientation preference is more likely to be inherited from the previous

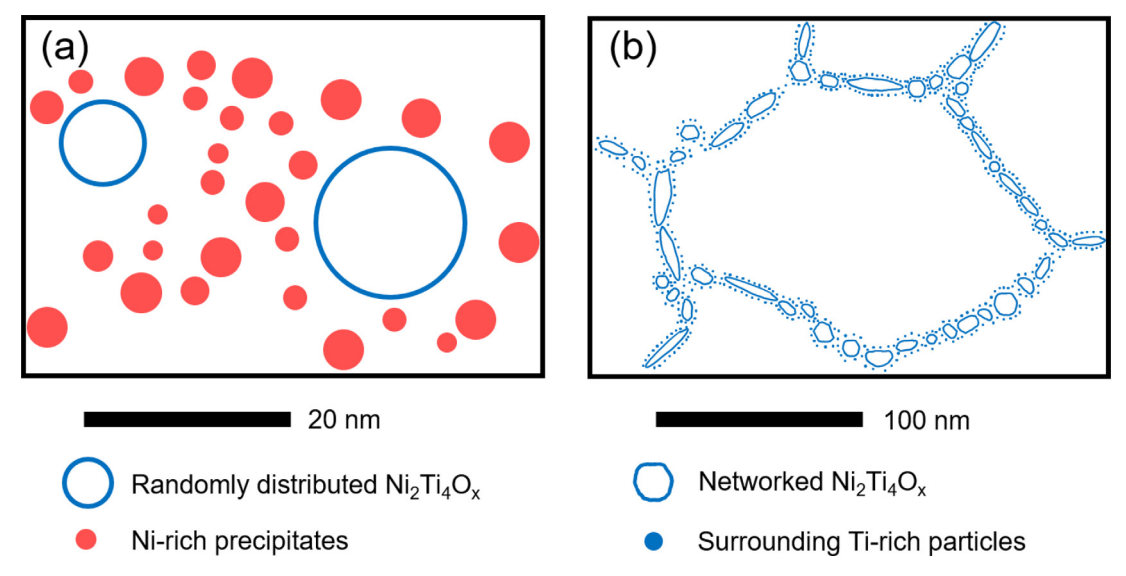


Fig. 21. Schematic of the precipitates and non-metallic inclusion particles observed in AM NiTi samples in this study. (a) Randomly distributed Ti-rich oxides surrounded by Ni-rich precipitates; (b) networked Ti-rich oxides surrounded by Ti-rich particles.

layer during cell growth since the <011> orientation parallel to the build direction will have a large angular deviation of 90°. Several studies [68, 71, 72] have shown successful control of the texture orientation in the AM parts in materials other than NiTi with different rotation angles. Therefore, a similar texture control should be possible in AM NiTi parts as well.

Evidently, the pseudo single crystal AM NiTi samples in the present study resulted from a combination of a shallow melt pool, a relatively small h value, and a 90° rotation angle between layers. Knowing the orientation selection/growth mechanism shall expand the scope of texture engineering in additively manufactured NiTi based SMAs as well as other materials with cubic crystal structure.

# 4.4. Effects of precipitates and inclusions on superelasticity and thermal transport of AM NiTi

As observed from the TEM images presented in Section 3.6, it is clear that the build chamber  $O_2$  level plays an important role in the formation of Ti-rich oxides. It is also likely that the high VED values (198 J/mm<sup>3</sup>) employed in this study exacerbated the oxidation as observed from the colored oxide layer formed on the rectangular prisms (Fig. 7).

As shown in Fig. 21, there are four types of particles observed in the AM NiTi samples based on the TEM study. Ultrafine Ni-rich precipitates (with a size range of 2-4 nm) were identified in the S100 material around the randomly distributed Ti-rich oxides in the grain interior. The depletion of Ti from the matrix due to the formation of Ti-rich oxides has dual effects: first, it increases the Ni/Ti ratio in the matrix, hence decreasing the transformation temperatures; second it promotes the formation of Ni-rich precipitates. Coherent nanosized Ni<sub>4</sub>Ti<sub>3</sub> precipitates are known to strongly influence the mechanical and shape memory properties of NiTi SMAs such as transformation temperatures [73], appearance of the intermediate R-phase transformation [74], functional and structural fatigue [65] and superelasticity [46, 75, 76]. In addition, the nanooxides should generate elastic strain fields in the surrounding area and serve as preferential nucleation sites for martensite at interfaces. All these nanosized particles strengthen the matrix by acting as barriers against slip deformation and potentially suppress the irreversibility associated with the martensitic transformation. It is likely that the presence of nanosized particles in the present AM samples (in addition to favourable crystallographic texture) re-

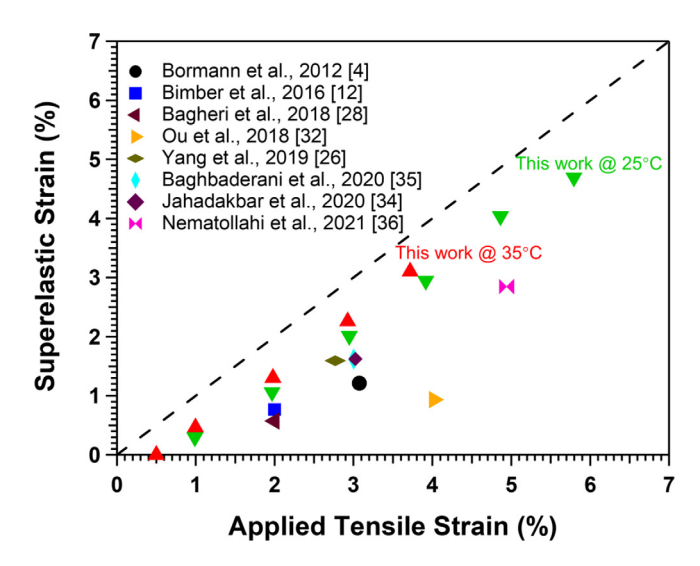


**Fig. 22.** Comparison of the tensile superelastic strain levels achieved in AM NiTi samples in the present work in comparison with what is reported in the literature so far.

sulted in the good superelastic behavior. On the other hand, there is a notably higher volume fraction of large oxide particles in the S500 samples, resulting in the inferior ductility and premature failure during the tension tests.

So far, there are only a few studies showing the existence of  $\mathrm{Ni_4Ti_3}$  type precipitates in AM NiTi in the as-printed condition [12, 77]. It is possible that the repetitive thermal cycling during the AM process is too fast to have enough time and preferable temperature for the growth of Ni-rich precipitates. It is also likely that the Ni-rich precipitates may be dissolved during the melting of subsequent layers. To the best of authors' knowledge, this is the first time that ultrafine Ni-rich precipitates with a size range of a few nanometres were identified in AM NiTi SMA. Most importantly, the highest superelastic strain achieved in this study is almost the double of what has been reported in the literature for AM NiTi (Fig. 22).

Based on the thermal diffusivity measurements, neither build chamber  $O_2$  level nor the measurement direction were found to have a significant impact on thermal conductivity values. There-

**Table 2** Transformation temperatures of  $Ni_{51.2}Ti_{48.8}$  samples showed in Fig. 6a and Fig. 6b. All transformation temperatures for the solution heat treated samples and those that can be determined with certainty for the as-printed samples are included.

Sample ID	M <sub>f</sub> (°C)	M <sub>s</sub> (°C)	A <sub>s</sub> (°C)	A <sub>f</sub> (°C)
As-Printed S500	-	-	-	27.1
Solutionized S500	-123.6	-63.2	-77.7	-13.9
As-Printed S100	-87.1	-	-17.8	23.7
Solutionized S100	-63.0	-27.7	-29.8	-0.1

fore, superelastic strain in AM NiTi can be increased as demonstrated here without a detrimental effect on thermal transport properties. Additionally, part orientation during printing does not have to be considered in order to optimize thermal transport, since thermal transport properties were not found to be anisotropic. Nevertheless, as a future work, a thorough systematic study is needed to evaluate the effects of different processing parameters on thermal transport properties to be able to fully implement AM NiTi parts in applications where the knowledge of thermal conductivity is significant, e.g. in the case of actuation applications, with the cycle time dependent on how quickly the SMA can cool down; or elastocaloric applications, where the heat absorbed or released during stress induced martensitic transformation should rapidly be transferred between different media for increased operation frequency.

## 5. Summary and Conclusions

In the present study, highly textured Ni-rich NiTi SMA parts were successfully fabricated without notable porosity or microcracks using the L-PBF technique and tensile superelasticity values up to 6% could be achieved through the selection of optimal processing parameters and formation of nanosized precipitates and oxide inclusions. The following summary statements and conclusions can be drawn:

- 1 The transformation temperatures increase with increasing volumetric energy density (VED) values due to the Ni evaporation during the AM process. Build chamber O<sub>2</sub> content notably influences the extent of oxidation that the printed parts experience. With increased O<sub>2</sub> content in the build chamber, the volume fraction of Ti-rich oxides increase, decreasing the transformation temperatures, acting opposite to the effect of Ni evaporation on transformation temperatures.
- 2 Crack and delamination issues observed in the printed parts may originate from the residual stresses generated due to the large thermal gradients during printing, and they were mitigated by using smaller hatch spacing and higher VED values. It is possible that with increased transformation temperatures and the initiation of the martensitic transformation when the printed parts cool down, residual stresses might be relaxed.
- 3 O<sub>2</sub> control of the atmosphere in the chamber was also found to be critical for the ductility of the printed parts and the achieved superelasticity levels. O<sub>2</sub> concentration of 500 ppm led to the parts that failed in a brittle manner at low strains without showing any sign of superelasticity, while decreasing the O<sub>2</sub> concentration to 100 ppm yielded parts that exhibit 6% superelastic strain without any post fabrication heat treatment, which is the highest reported to date in literature.
- 4 The unique AM microstructure with strong texture, the presence of nano-sized inclusions and ultrafine Ni-rich precipitates suggest a possible approach for achieving high levels superelasticity in AM NiTi in the as-fabricated condition. Thermal history during the process needs to be further studied in order to provide the ideal conditions for the growth of Ni-rich precipi-

- tates, otherwise post heat treatments may be necessary for the achievement of superelasticity.
- 5 The strong favourable crystallographic texture in the as-printed tension samples indicated that the superelastic properties are orientation dependent. Hence, further engineering the texture may favor better mechanical properties (i.e. strength and superelasticity level) for the near-net-shape fabrication of complex functional NiTi parts.
- 6 Thermal conductivity values of the as-printed NiTi were found to be independent of the build chamber O<sub>2</sub> level, in the range studied in the present study, or orientation of the part. As a future work, a more detailed study is required to characterize the effects of processing parameters such as laser power, scan speed and hatch spacing for a complete understanding of the relationship between microstructure and thermal transport properties in AM NiTi.

#### **Data Availability Statement**

The data that support the findings of this study are available from the corresponding author, [IK], upon reasonable request.

## **Declaration of Competing Interest**

The authors declare that they have no known competing financial interests or personal relationships that could have appeared to influence the work reported in this paper.

#### Acknowledgments

The authors would like to acknowledge the financial support from U.S. Army Research Laboratory through cooperative agreement No. W911NF1920264. L. Xue acknowledges the support from the National Priorities Research Program grant, NPRP12-S No: 0131-190029, from the Qatar National Research Fund (a member of The Qatar Foundation). A. Elwany acknowledges the support from U.S. National Science Foundation Grant No. 1846676. The statements made herein are solely the responsibility of the authors.

#### References

- E. Kaya, İ. Kaya, A review on machining of NiTi shape memory alloys: the process and post process perspective, The International Journal of Advanced Manufacturing Technology 100 (5) (2019) 2045–2087.
- [2] H.C. Lin, K.M. Lin, Y.C. Chen, A study on the machining characteristics of TiNi shape memory alloys, Journal of Materials Processing Technology 105 (3) (2000) 327–332.
- [3] K. Weinert, V. Petzoldt, Machining of NiTi based shape memory alloys, Materials Science and Engineering A 378 (1-2) (2004) 180–184.
- [4] T. Bormann, R. Schumacher, B. Mueller, M. Mertmann, M. de Wild, Tailoring Selective Laser Melting Process Parameters for NiTi Implants, Journal of Materials Engineering and Performance 21 (12) (2012) 2519–2524.
- [5] S. Dadbakhsh, M. Speirs, J. Van Humbeeck, J.-P. Kruth, Laser additive manufacturing of bulk and porous shape-memory NiTi alloys: From processes to potential biomedical applications, MRS Bulletin 41 (10) (2016) 765–774.
- [6] S. Dadbakhsh, B. Vrancken, J.P. Kruth, J. Luyten, J. Van Humbeeck, Texture and anisotropy in selective laser melting of NiTi alloy, Materials Science and Engineering A 650 (2016) 225–232.
- [7] C. Haberland, H. Meier, J. Frenzel, Asme, On the Properties of Ni-rich NiTi Shape Memory Parts Produced by Selective Laser Melting, in: Proceedings of the ASME 2012 Conference on Smart Materials, Adaptive Structures and Intelligent Systems, Volume 1: Development and Characterization of Multifunctional Materials; Modeling, Simulation and Control of Adaptive Systems; Structural Health Monitoring, Stone Mountain, Georgia, USA. September 19–21, ASME2012, 2012, pp. 97–104.
- [8] M.D. Hayat, G. Chen, N. Liu, S. Khan, H.P. Tang, P. Cao, Physical and Tensile Properties of NiTi Alloy by Selective Electron Beam Melting, Key Engineering Materials 770 (2018) 148–154.
- [9] J. Ma, B. Franco, G. Tapia, K. Karayagiz, L. Johnson, J. Liu, R. Arroyave, I. Karaman, A. Elwany, Spatial Control of Functional Response in 4D-Printed Active Metallic Structures, Scientific Reports 7 (2017).
- [10] S. Saedi, A.S. Turabi, M.T. Andani, C. Haberland, H. Karaca, M. Elahinia, The influence of heat treatment on the thermomechanical response of Ni-rich NiTi alloys manufactured by selective laser melting, Journal of Alloys and Compounds 677 (2016) 204–210.

[11] Q. Zhou, M.D. Hayat, G. Chen, S. Cai, X. Qu, H. Tang, P. Cao, Selective electron beam melting of NiTi: Microstructure, phase transformation and mechanical properties, Materials Science and Engineering A 744 (2019) 290–298.

- [12] B.A. Bimber, R.F. Hamilton, J. Keist, T.A. Palmer, Anisotropic microstructure and superelasticity of additive manufactured NiTi alloy bulk builds using laser directed energy deposition, Materials Science and Engineering A 674 (2016) 125–134.
- [13] B.A. Bimber, R.F. Hamilton, T.A. Palmer, Ni-Concentration Dependence of Directed Energy Deposited NiTi Alloy Microstructures, Shape Memory and Superelasticity 5 (2) (2019) 182–187.
   [14] M. Das, V.K. Balla, T.S.S. Kumar, I. Manna, Fabrication of Biomedical Implants
- [14] M. Das, V.K. Balla, T.S.S. Kumar, I. Manna, Fabrication of Biomedical Implants using Laser Engineered Net Shaping (LENS (TM)), Transactions of the Indian Ceramic Society 72 (3) (2013) 169–174.
- [15] R.F. Hamilton, B.A. Bimber, T.A. Palmer, Correlating microstructure and superelasticity of directed energy deposition additive manufactured Ni-rich NiTi alloys, Journal of Alloys and Compounds 739 (2018) 712–722.
- [16] R.F. Hamilton, T.A. Palmer, B.A. Bimber, Spatial characterization of the thermal-induced phase transformation throughout as-deposited additive manufactured NiTi bulk builds, Scripta Materialia 101 (2015) 56–59.
- [17] S. Shiva, I.A. Palani, S.K. Mishra, C.P. Paul, L.M. Kukreja, Investigations on the influence of composition in the development of Ni-Ti shape memory alloy using laser based additive manufacturing, Optics and Laser Technology 69 (2015) 44-51.
- [18] C. Wang, X.P. Tan, Z. Du, S. Chandra, Z. Sun, C.W.J. Lim, S.B. Tor, C.S. Lim, C.H. Wong, Additive manufacturing of NiTi shape memory alloys using pre-mixed powders, Journal of Materials Processing Technology 271 (2019) 152-161.
- [19] T. Habijan, C. Haberland, H. Meier, J. Frenzel, J. Wittsiepe, C. Wuwer, C. Greulich, T.A. Schildhauer, M. Koeller, The biocompatibility of dense and porous Nickel-Titanium produced by selective laser melting, Materials Science & Engineering C-Materials for Biological Applications 33 (1) (2013) 419–426.
- [20] X. Wang, J. Yu, J. Liu, L. Chen, Q. Yang, H. Wei, J. Sun, Z. Wang, Z. Zhang, G. Zhao, J. Van Humbeeck, Effect of process parameters on the phase transformation behavior and tensile properties of NiTi shape memory alloys fabricated by selective laser melting, Additive Manufacturing 36 (2020) 101545.
- [21] T. Bormann, B. Mueller, M. Schinhammer, A. Kessler, P. Thalmann, M. de Wild, Microstructure of selective laser melted nickel-titanium, Materials Characterization 94 (2014) 189–202.
- [22] M. Elahinia, N.S. Moghaddam, M.T. Andani, A. Amerinatanzi, B.A. Bimber, R.F. Hamilton, Fabrication of NiTi through additive manufacturing: A review, Progress in Materials Science 83 (2016) 630–663.
- [23] C. Haberland, M. Elahinia, J.M. Walker, H. Meier, J. Frenzel, On the development of high quality NiTi shape memory and pseudoelastic parts by additive manufacturing, Smart Materials and Structures 23 (10) (2014) 104002.
- [24] J. Sam, B. Franco, J. Ma, I. Karaman, A. Elwany, J.H. Mabe, Tensile actuation response of additively manufactured nickel-titanium shape memory alloys, Scripta Materialia 146 (2018) 164–168.
- [25] M. Speirs, X. Wang, S. Van Baelen, A. Ahadi, S. Dadbakhsh, J.P. Kruth, J. Van Humbeeck, On the Transformation Behavior of NiTi Shape-Memory Alloy Produced by SLM, Shape Memory and Superelasticity 2 (4) (2016) 310–316.
- [26] Y. Yang, J.B. Zhan, B. Li, J.X. Lin, J.J. Gao, Z.Q. Zhang, L. Ren, P. Castany, T. Gloriant, Laser beam energy dependence of martensitic transformation in SLM fabricated NiTi shape memory alloy, Materialia 6 (2019) 100305.
- [27] B.E. Franco, J. Ma, B. Loveall, G.A. Tapia, K. Karayagiz, J. Liu, A. Elwany, R. Arroyave, I. Karaman, A Sensory Material Approach for Reducing Variability in Additively Manufactured Metal Parts, Sci Rep 7 (1) (2017) 3604.
- [28] A. Bagheri, M.J. Mahtabi, N. Shamsaei, Fatigue behavior and cyclic deformation of additive manufactured NiTi, Journal of Materials Processing Technology 252 (2018) 440-453
- [29] A. Jahadakbar, M. Nematollahi, K. Safaei, P. Bayati, G. Giri, H. Dabbaghi, D. Dean, M. Elahinia, Design, Modeling, Additive Manufacturing, and Polishing of Stiffness-Modulated Porous Nitinol Bone Fixation Plates Followed by Thermomechanical and Composition Analysis, Metals 10 (1) (2020) 151.
- [30] Keyvan Safaei Baghbaderani, Mohammadreza Nematollahi, Parisa Bayatimalayeri, Hediyeh Dabbaghi, Ahmadreza Jahadakbar, M. Elahinia, Mechanical Evaluation of Selective Laser Melted Ni-Rich NiTi: Compression, Tension, And Torsion, in: Proceedings of the ASME 2020 15th International Manufacturing Science and Engineering Conference. Volume 1: Additive Manufacturing; Advanced Materials Manufacturing; Biomanufacturing; Life Cycle Engineering; Manufacturing Equipment and Automation. Virtual, Online, ASME2020, September 3, 2020 MSEC2020-8432, V001T01A019.
- [31] N.S. Moghaddam, S. Saedi, A. Amerinatanzi, A. Hinojos, A. Ramazani, J. Kundin, M.J. Mills, H. Karaca, M. Elahinia, Achieving superelasticity in additively manufactured NiTi in compression without post-process heat treatment, Scientific Reports 9 (2019).
- [32] S.-F. Ou, B.-Y. Peng, Y.-C. Chen, M.-H. Tsai, Manufacturing and Characterization of NiTi Alloy with Functional Properties by Selective Laser Melting, Metals 8 (5) (2018).
- [33] Y. Yang, J.B. Zhan, Z.Z. Sun, H.L. Wang, J.X. Lin, Y.J. Liu, L.C. Zhang, Evolution of functional properties realized by increasing laser scanning speed for the selective laser melting fabricated NiTi alloy, Journal of Alloys and Compounds 804 (2019) 220–229.
- [34] A. Jahadakbar, M. Nematollahi, K. Safaei, P. Bayati, G. Giri, H. Dabbaghi, D. Dean, M.J.M. Elahinia, Design, modeling, additive manufacturing, and polishing of stiffness-modulated porous nitinol bone fixation plates followed by thermomechanical and composition analysis 10 (1) (2020) 151.

[35] K.S. Baghbaderani, M. Nematollahi, P. Bayatimalayeri, H. Dabbaghi, A. Jahadak-bar, M.J.a.p.a. Elahinia, Mechanical Evaluation Of Selective Laser Melted Ni-Rich Niti: Compression, Tension, And Torsion (2020).

- [36] M. Nematollahi, S.E. Saghaian, K. Safaei, P. Bayati, P. Bassani, C. Biffi, A. Tuissi, H. Karaca, M. Elahinia, Building orientation-structure-property in laser powder bed fusion of NiTi shape memory alloy, Journal of Alloys and Compounds 873 (2021).
- [37] L. Xue, K.C. Atli, S. Picak, C. Zhang, B. Zhang, A. Elwany, R. Arroyave, I. Karaman, Controlling martensitic transformation characteristics in defect-free NiTi shape memory alloys fabricated using laser powder bed fusion and a process optimization framework, Acta Materialia 215 (2021) 117017.
- [38] Z. Xiong, Z. Li, Z. Sun, S. Hao, Y. Yang, M. Li, C. Song, P. Qiu, L. Cui, Selective laser melting of NiTi alloy with superior tensile property and shape memory effect, Journal of Materials Science & Technology 35 (10) (2019) 2238–2242.
   [39] A. International, F2063-05 StandardSpecification for Wrought Nickel-Titanium
- [39] A. International, F2063-05 StandardSpecification for Wrought Nickel-Titanium Shape Memory Alloys for Medical Devices and Surgical Implants, ASTM International, 2005.
- [40] H. Sehitoglu, I. Karaman, R. Anderson, X. Zhang, K. Gall, H.J. Maier, Y. Chumlyakov, Compressive response of NiTi single crystals, Acta Materialia 48 (13) (2000) 3311–3326.
- [41] K. Gall, H. Sehitoglu, R. Anderson, I. Karaman, Y.I. Chumlyakov, I.V. Kireeva, On the mechanical behavior of single crystal NiTi shape memory alloys and related polycrystalline phenomenon, Materials Science and Engineering A 317 (1-2) (2001) 85–92.
- [42] Y.I. Chumlyakov, I.V. Kireeva, E.Y. Panchenko, E.E. Timofeeva, Z.V. Pobedennaya, S.V. Chusov, I. Karaman, H. Maier, E. Cesari, V.A. Kirillov, High-temperature superelasticity in CoNiGa, CoNiAl, NiFeGa, and TiNi monocrystals, Russ Phys J+ 51 (10) (2008) 1016–1036.
- [43] C.A. Biffi, J. Fiocchi, F. Valenza, P. Bassani, A. Tuissi, Selective Laser Melting of NiTi Shape Memory Alloy: Processability, Microstructure, and Superelasticity, Shape Memory and Superelasticity 6 (3) (2020) 342–353.
- [44] B. Franco, Engineering the martensitic transformation hysteresis of Ni-rich NiTi alloys, Texas A&M University, 2014.
- [45] D. Favier, Y. Liu, L. Orgeas, A. Sandel, L. Debove, P. Comte-Gaz, Influence of thermomechanical processing on the superelastic properties of a Ni-rich Nitinol shape memory alloy, Materials Science and Engineering A 429 (1-2) (2006) 130–136.
- [46] F. Jiang, Y. Liu, H. Yang, L. Li, Y. Zheng, Effect of ageing treatment on the deformation behaviour of Ti-50.9 at.% Ni, Acta Materialia 57 (16) (2009) 4773-4781.
- [47] X. Liu, Y. Wang, D. Yang, M. Qi, The effect of ageing treatment on shape-setting and superelasticity of a nitinol stent, Materials Characterization 59 (4) (2008) 402–406.
- [48] H. Mohamad, A.S. Mahmud, M.N. Nashrudin, M.F. Razali, Effect of Ageing Temperatures on Pseudoelasticity of Ni-rich NiTi Shape Memory Alloy, in: H. Metselaar, W.Y. Hoong, R. Mahmoodian, M.F. Jamaludin (Eds.), 3rd International Conference on the Science and Engineering of Materials, 2018.
- [49] A. Sinha, B. Mondal, P.P. Chattopadhyay, Mechanical properties of Ti-(similar to 49 at%) Ni shape memory alloy, part II: Effect of ageing, Materials Science and Engineering A 561 (2013) 344–351.
- [50] C. Haberland, M. Elahinia, J. Walker, H. Meier, J. Frenzel, Asme, Additive Manufacturing of Shape Memory Devices and Pseudoelastic Components, in: Proceedings of the ASME 2013 Conference on Smart Materials, Adaptive Structures and Intelligent Systems. Volume 1: Development and Characterization of Multifunctional Materials; Modeling, Simulation and Control of Adaptive Systems; Integrated System Design and Implementation. Snowbird, Utah, USA. September 16–18, ASME2014, 2013 V001T01A005.
- [51] R. Seede, D. Shoukr, B. Zhang, A. Whitt, S. Gibbons, P. Flater, A. El-wany, R. Arroyave, I. Karaman, An ultra-high strength martensitic steel fabricated using selective laser melting additive manufacturing: Densification, microstructure, and mechanical properties, Acta Materialia 186 (2020) 199–214.
- [52] T.W. Eagar, N.S. Tsai, Temperature Fields Produced by Traveling Distributed Heat Sources, Welding Journal 62 (12) (1983) \$346-\$355.
- [53] A. International, F2004-17 Standard Test Method for Transformation Temperature of Nickel-Titanium Alloys by Thermal Analysis, ASTM International, West Conshohocken, PA, 2017.
- [54] A. International, B962-17 Standard Test Methods for Density of Compacted or Sintered Powder Metallurgy (PM) Products Using Archimedes' Principle, ASTM International, West Conshohocken, PA, 2017.
- [55] J. Frenzel, A. Wieczorek, I. Opahle, B. Maass, R. Drautz, G. Eggeler, On the effect of alloy composition on martensite start temperatures and latent heats in Ni-Ti-based shape memory alloys, Acta Materialia 90 (2015) 213–231.
- [56] J. Frenzel, E.P. George, A. Dlouhy, C. Somsen, M.F.X. Wagner, G. Eggeler, Influence of Ni on martensitic phase transformations in NiTi shape memory alloys, Acta Materialia 58 (9) (2010) 3444–3458.
- [57] S. Zhang, B.R. Xue, L. Atli, K.C. Zhang, C. Whitt, A. Karaman, I. Arroyave, R. El-wany A, An Efficient Framework for Printability Assessment in Laser Powder Bed Fusion Metal Additive Manufacturing, Additive Manufacturing 46 (2021) 107018
- [58] F. Cheng, L. Hu, J.N. Reddy, I. Karaman, E. Hoffman, M. Radovic, Temperature-dependent thermal properties of a shape memory alloy/MAX phase composite: Experiments and modeling. Acta Materialia 68 (2014) 267–278.
- posite: Experiments and modeling, Acta Materialia 68 (2014) 267–278.

  [59] B.D. Ingale, W.C. Wei, P.C. Chang, Y.K. Kuo, S.K. Wu, Anomalous transport and thermal properties of NiTi and with Cu and Fe-doped shape memory alloys near the martensitic transition, Journal of Applied Physics 110 (11) (2011).

[60] M. Bram, M. Bitzer, H.P. Buchkremer, D. Stover, Reproducibility Study of NiTi Parts Made by Metal Injection Molding, Journal of Materials Engineering and Performance 21 (12) (2012) 2701–2712.

- [61] L.A. Parry, I.A. Ashcroft, R.D. Wildman, Geometrical effects on residual stress in selective laser melting, Additive Manufacturing 25 (2019) 166–175.
- [62] B. Cheng, S. Shrestha, K.V. Chou, Stress and deformation evaluations of scanning strategy effect in selective laser melting, Additive Manufacturing 12 (2016) 240-251.
- [63] S. Miyazaki, Y. Kohiyama, K. Otsuka, T.W. Duerig, Effects of Several Factors on the Ductility of the Ti-Ni Alloy, Materials Science Forum 56-58 (1990) 765-770.
  [64] K. Gall, H. Sehitoglu, Y.I. Chumlyakov, I.V. Kireeva, Tension-compression asym-
- [64] K. Gall, H. Sehitoglu, Y.I. Chumlyakov, I.V. Kireeva, Tension-compression asymmetry of the stress-strain response in aged single crystal and polycrystalline NiTi, Acta Materialia 47 (4) (1999) 1203–1217.
- [65] K. Gall, N. Yang, H. Sehitoglu, Y.I. Chumlyakov, Fracture of precipitated NiTi shape memory alloys, International Journal of Fracture 109 (2) (2001) 189–207.
- [66] S.R. Suwas, Ranjit Kumar, Crystallographic Texture of Materials, Springer, 2014.
- [67] O. Andreau, I. Koutiri, P. Peyre, J.-D. Penot, N. Saintier, E. Pessard, T. De Terris, C. Dupuy, T. Baudin, Texture control of 316L parts by modulation of the melt pool morphology in selective laser melting, Journal of Materials Processing Technology 264 (2019) 21–31.
- [68] K.A. Sofinowski, S. Raman, X. Wang, B. Gaskey, M. Seita, Layer-wise engineering of grain orientation (LEGO) in laser powder bed fusion of stainless steel 316L, Additive Manufacturing 38 (2021).
- [69] S.-H. Sun, T. Ishimoto, K. Hagihara, Y. Tsutsumi, T. Hanawa, T. Nakano, Excellent mechanical and corrosion properties of austenitic stainless steel with a unique crystallographic lamellar microstructure via selective laser melting, Scripta Materialia 159 (2019) 89–93.

[70] C.A. Biffi, P. Bassani, J. Fiocchi, A. Tuissi, Microstructural and Mechanical Response of NiTi Lattice 3D Structure Produced by Selective Laser Melting, Metals 10 (6) (2020).

- [71] R.R. Dehoff, M.M. Kirka, W.J. Sames, H. Bilheux, A.S. Tremsin, L.E. Lowe, S.S. Babu, Site specific control of crystallographic grain orientation through electron beam additive manufacturing, Materials Science and Technology 31 (8) (2015) 931–938.
- [72] F. Geiger, K. Kunze, T. Etter, Tailoring the texture of IN738LC processed by selective laser melting (SLM) by specific scanning strategies, Materials Science and Engineering A 661 (2016) 240–246.
- [73] E.Y. Panchenko, Y.I. Chumlyakov, I.V. Kireeva, A.V. Ovsyannikov, H. Sehitoglu, I. Karaman, Y.H.J. Maier, Effect of disperse Ti3N4 particles on the martensitic transformations in titanium nickelide single crystals, Physics of Metals and Metallography 106 (6) (2008) 577–589.
- [74] J.I. Kim, Y.N. Liu, S. Miyazaki, Ageing-induced two-stage R-phase transformation in Ti-50.9at.%Ni, Acta Materialia 52 (2) (2004) 487–499.
  [75] Y.I. Chumlyakov, S.P. Efimenko, I.V. Kireeva, E.Y. Panchenko, H. Sehitogly,
- [75] Y.I. Chumlyakov, S.P. Efimenko, I.V. Kireeva, E.Y. Panchenko, H. Sehitogly, K. Gall, L.H. Yahia, Effects of shape memory and superelasticity in aged TiNi single crystals, Doklady Physics 46 (12) (2001) 849–852.
- [76] H. Sehitoglu, J. Jun, X. Zhang, I. Karaman, Y. Chumlyakov, H.J. Maier, K. Gall, Shape memory and pseudoelastic behavior of 51.5%Ni-Ti single crystals in solutionized and overaged state. Acta Materialia 49 (17) (2001) 3609–3620.
- lutionized and overaged state, Acta Materialia 49 (17) (2001) 3609–3620.
   J. Gan, L. Duan, F. Li, Y. Che, Y. Zhou, S. Wen, C. Yan, Effect of laser energy density on the evolution of Ni<sub>4</sub>Ti<sub>3</sub> precipitate and property of NiTi shape memory alloys prepared by selective laser melting, Journal of Alloys and Compounds 869 (2021) 159338.